Computational Modeling of a Solar Thermoelectric Generator

Undergraduate Thesis

Presented in Partial Fulfillment of the Requirements for Graduation with Research Distinction at The Ohio State University

By: Chukwunyere Ofoegbu

Advisor: Professor Sandip Mazumder

The Ohio State University

Department of Mechanical and Aerospace Engineering

Defense Committee:

Dr. Sandip Mazumder, Advisor

Dr. Joseph P. Heremans

April 2014

Abstract

Solar to electrical power conversion technologies have become a popular alternative to conventional means such as combustion of fossil fuels because no greenhouse gases are produced. One of the emerging technologies is a solar thermoelectric power generation. A solar thermoelectric generator (STEG) converts radiant energy from the sun into electricity by creating a temperature difference across a thermoelectric material. The solar energy is first absorbed by an absorber plate that heats up and creates the afore-mentioned temperature difference. As opposed to solar photovoltaic cells that utilize only the visible part of the sun's energy spectrum, a STEG utilizes the entire energy spectrum—most notably the infrared part. This noteworthy advantage makes this technology promising. Advancements in thermoelectric material research have proved that STEGs are a viable option for small scale power generation. Currently, the measured efficiency of STEGs is very low (less than 1%). This low efficiency is presumably caused by excessive heat loss by the absorber plate to the ambient, resulting in a low temperature gradient across the thermoelectric device. In this research, in an effort to understand the mechanisms of heat loss, a detailed computational study of a STEG was performed to understand the effects of various operating conditions on the efficiency of the device. A coupled thermal-electric three-dimensional simulations was performed under operating conditions similar to a recently conducted experimental study. The results obtained in this study showed that heat loss by natural convection is the dominant cause of low temperature gradients. The numerical study predicted an efficiency of 0.0884%, which was 47 times less than the efficiency without the effects of natural convection. The results of this study were validated against experimental results for operations in vacuum and operations in atmospheric conditions respectively.

Acknowledgments

This thesis could not have been written without the great support from Dr. Sandip Mazumder, who not only served as my research advisor but also played a tremendous role in encouraging and challenging me throughout the course of this research. I also want to thank The Undergraduate Honors Committee in the College of Engineering for supporting my research with the Undergraduate Research scholarship award.

I thank ESI Group, North America for providing free licenses to CFD-ACE+^{TM}, which was used extensively in this research. Finally, a special thanks to my family and friends for their loving and encouraging support.

Table of Contents

List of Figures

List of Tables

Chapter 1
Introduction

1.1 Technology Background

The conversion of solar energy into electricity has been dependent on two methods. One is the use of solar photovoltaic cells, which convert photon energy into electricity [1]. The other is solar-thermal that converts photon energy into a terrestrial heat source, usually through optical concentrators, and uses mechanical heat engines to generate electricity [2,3]. Solar thermoelectric technology substitutes the mechanical heat engines in solar-thermal systems with a solid-state thermoelectric generator. Thermoelectric generators rely on the Seebeck effect in solid materials to convert thermal energy into electricity [4]. By replacing the mechanical heat engines with thermoelectric generators, the advantages of solar thermoelectric generator (STEG) cells become similar to those of photovoltaic cells.

The basic design of a solar thermoelectric generator is shown in Figure 1-1 [5]. Here a thermoelectric module is placed between two plates. The top plate (hot reservoir) is coated with a highly absorbent material and is exposed to the sun to heat up. The bottom plate (cold reservoir) is kept at ambient temperatures. The temperature difference between the top and bottom plates creates a voltage difference within the thermoelectric elements, by virtue of the Seebeck effect [4]. Solar thermoelectric generators pose an advantage over photovoltaic cells in their ability to utilize the energy from the entire spectrum of the sun [5], unlike photovoltaic cells that only absorb the energy from visible photons, which is only 36% of the sun's energy [6].

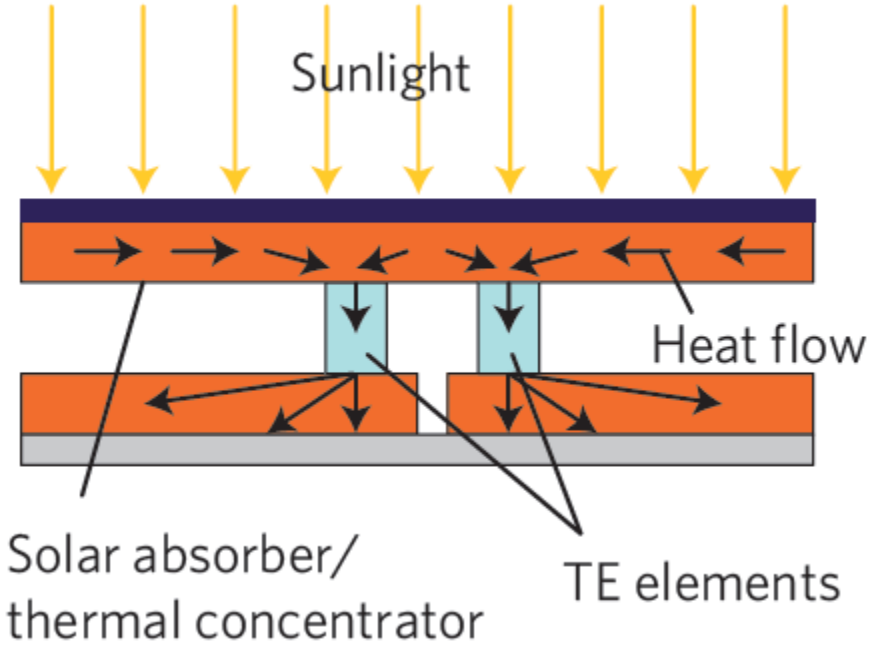

Figure 1-1: Schematic of a Solar Thermoelectric Generator

1.2 Previous Work

A recent experimental study performed by Sarah Watzman [7] achieved a peak STEG efficiency of 0.0582%. This study used a flat-plate solar absorber design as shown in Figure 1-2.

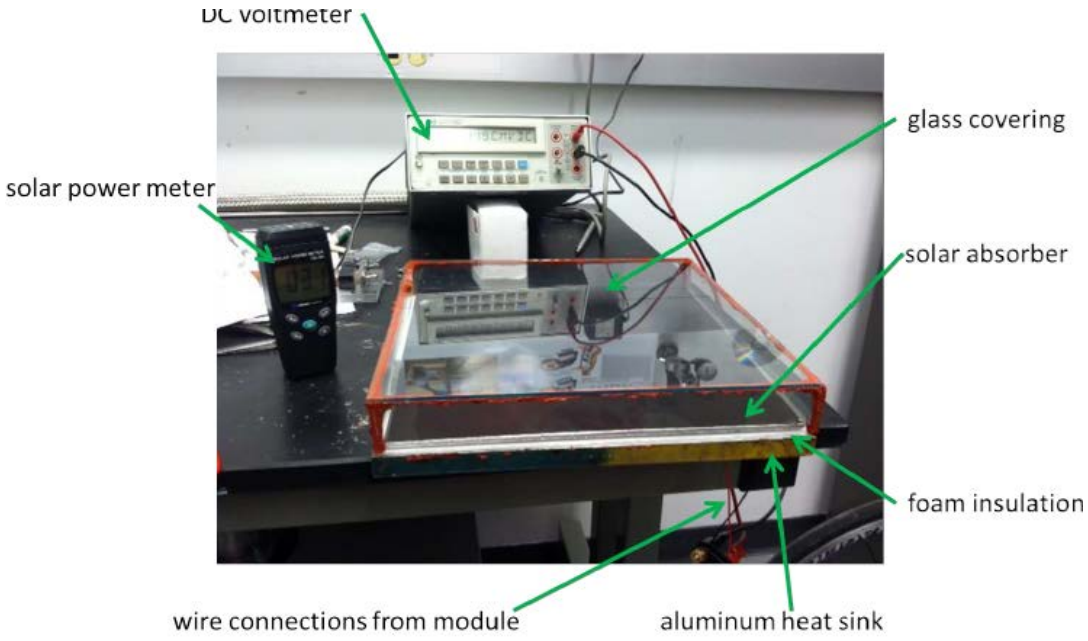

Figure 1-2: Experimental Set-Up

Here, a glass covering was used to eliminate any heat losses from the absorber plate by forced convection during the operation of the device outdoors. A thermoelectric module shown in Figure 1-3 was used in this experiment.

Figure 1-3: Thermoelectric Module Used in Experiment

Figure 1-4 shows a schematic illustrating how thermoelectric modules work. Thermoelectric modules consist of two dissimilar thermoelectric elements arranged electrically in series, and thermally in parallel. A set of two dissimilar legs forms a unicouple. With the arrangement in Figure 1-4, the voltage produced in one leg of the unicouple, on exposure to a temperature gradient, is added to the voltage produced in the other leg. In this way the net voltage produced by the thermoelectric module is the product of the number of unicouples and the voltage per unicouple.

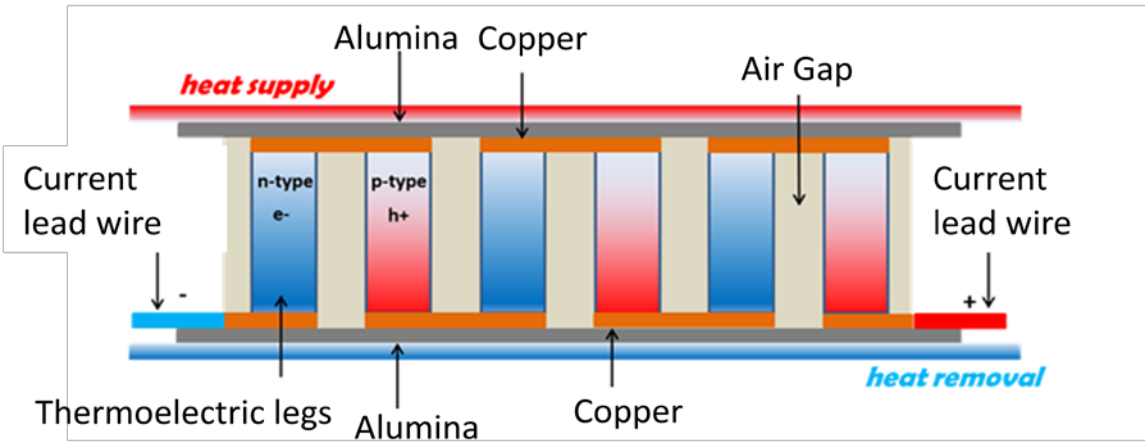

Figure 1-4: Schematic of a Thermoelectric Module

The thermoelectric module was attached to the bottom of the absorber plate, shown in Figure 1-5. By using an absorber plate area much larger than the area of the thermoelectric module, the heat source is concentrated on the thermoelectric elements which effectively increase the temperature gradient.

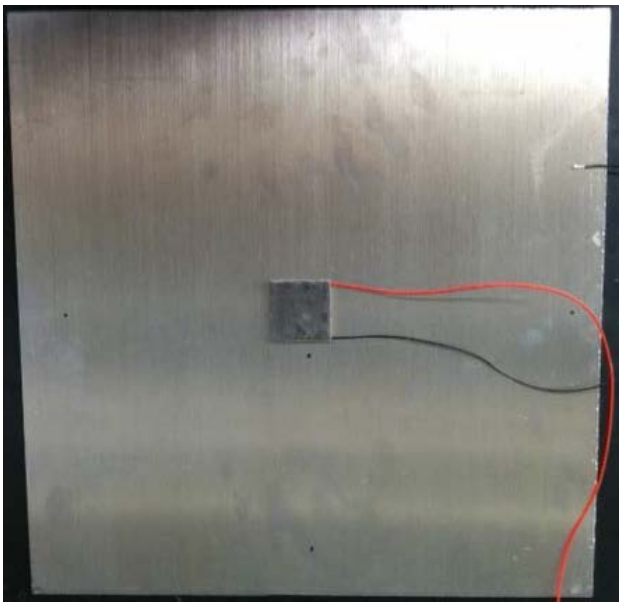

Figure 1-5: Attachment of the Thermoelectric Module to the Absorber Plate

The dimensions of the STEG are summarized in Table 1.

Table 1: Dimensions of STEG Components

Component	Material Type	Dimensions [L x W x H] (mm)
Absorber Plate	Aluminum	292.1 x 292.1 x 4.7625
Thermoelectric Module (Layer)	Alumina	35 x 35 x 1.175
Thermoelectric Unicouple (126 legs)	Bismuth-Telluride	1.29 x 1.29 x 1.5
Heat Sink	Aluminum	304.8 x 304.8 x 15.875

The results of outdoor tests performed in the experiment are summarized in Table 2.

Table 2: Loaded Test Results for Outdoor Tests

	Loaded Test 1	Loaded Test 2
Measured Solar Flux (W/m^2)	834	750
Input Solar Power* (W)	36.48	32.81
Open Circuit Voltage (V)	0.660	0.640
Maximum Power Output (W)	0.0209	0.0191
Peak System Efficiency*	0.05736%	0.0582%
Estimated Ambient Temperature (K)	278.7	278.7

* The input solar power was calculated by multiplying the measured solar flux in each case by the area of the absorber plate, the transmissivity of the glass cover, the emissivity of the absorber plate coating, and the estimated cosine of the solar zenith angle for Latitude 40 N in March when the experiment was performed.

The computational model described in this thesis was developed using the information from Watzman's experimental study [7].

1.3 Motivation for Current Research

Despite the potential for STEGs in power generation, they are not widely used because they have a low efficiency. Thus, photovoltaic cells dominate the category of solar to electric conversion devices as they have a higher efficiency. Currently, the maximum efficiency obtained experimentally is approximately 5.2% when operated in vacuum [5]. Under operations in air, the efficiency is even much lower at .060% [7]. This lower efficiency is presumably caused by convective heat losses from exposure to air, leading to a lower temperature gradient across the thermoelectric device.

Since the efficiency of STEGs depend on the temperature gradient across the thermoelectric elements, there is the need for an effective thermal management in the design of

these devices. An optimized temperature gradient can only be achieved through a thorough investigation of the thermal behavior of the device under atmospheric operation. This investigation can be done through high fidelity computational modeling of the entire system under atmospheric conditions. The knowledge gained from the computational study will reveal areas where heat losses occur, and what design strategies could be adopted to curtail the heat losses.

1.4 Objectives

The objectives of this research are as follows;

- To develop a coupled fluid-thermal-electric three-dimensional CFD model of a solar thermoelectric energy conversion unit.
- To explore the effects of different operating conditions on the performance of the model.
- To validate the CFD model against the experimental data described in Chapter 1.2.

1.5 Organization of Thesis

This thesis is divided into four chapters; Chapter 1 discusses the introduction of STEGs, previous research on STEGs, and motivation for this research. Chapter 2 describes the research methods used, including the governing equations and the parameters of the simulation used in the commercial software *CFD-ACE+*™ [8]. Chapter 3 discusses the results obtained, as well as the validation of the numerical solutions. Finally, Chapter 4 discusses the summary and conclusion, as well as recommendations for further work.

Chapter 2
Research Method

2.1 Governing Equations

The numerical analysis was performed using the governing equations presented below. These equations are solved using the Finite Volume Method (FVM) by a commercial multiphysics software CFD-ACE^{TM}. The governing equations are expressed in vectorial form below [9];

Conservation of Mass: $\frac{\partial}{\partial t}(\rho) + \nabla.(\rho\mathbf{U}) = \mathbf{0}$ (2.1)

Conservation of Momentum: $\frac{\partial}{\partial t}(\rho\mathbf{U}) + \nabla.(\rho\mathbf{UU}) = -\nabla\rho + \nabla.(\mu\nabla\mathbf{U}) + \rho\mathbf{B}$ (2.2)

Conservation of Energy: $\frac{\partial}{\partial t}(\rho \mathrm{h}) + \nabla.(\rho\mathbf{U}h) = -\nabla.\mathbf{q} + \frac{\partial p}{\partial t} + \mathbf{U}.\nabla \mathrm{p} + \nabla\mathbf{U}:\boldsymbol{\tau} + \dot{\mathrm{Q}}_{\mathrm{gen}}$ (2.3)

Heat Flow: $\rho C\frac{\partial}{\partial t}(T) + \nabla.\mathbf{q} = \dot{\mathrm{Q}}_{\mathrm{gen}}$ (2.4)

Continuity of Electric Charge: $\nabla.\left(\boldsymbol{J} + \frac{\partial \boldsymbol{D}}{\partial t}\right) = 0$ (2.5)

Equations 2.4 and 2.5 are coupled to give the following set of thermoelectric equations;

$$\mathbf{q} = \mathrm{T}[\alpha].\boldsymbol{J} - [\boldsymbol{\lambda}].\nabla T \quad (2.6)$$

$$\boldsymbol{J} = [\sigma].(\boldsymbol{E} - [\alpha].\nabla T) \quad (2.7)$$

$$where\ \boldsymbol{E} = -\nabla\varphi$$

Where ρ is the density, **U** is the velocity vector, μ is the fluid dynamic viscosity, **B** is the body force vector, h is the specific enthalpy, **q** is the heat flux vector, p is the fluid pressure, $\boldsymbol{\tau}$ is the shear force vector, $\dot{\mathrm{Q}}_{\mathrm{gen}}$ is the heat generation rate, *C* is the specific heat, T is the absolute

temperature, $\boldsymbol{J}$ is the current density vector, $\boldsymbol{D}$ is the electric flux density vector, [α] is the Seebeck coefficient matrix, [$\boldsymbol{\lambda}$] is the thermal conductivity matrix, [σ] is the thermal conductivity matrix, $\boldsymbol{E}$ is the electric field intensity vector, and is the electric scalar potential.

These governing equations are only applicable to select computational domains. Equation (2.1) and (2.2) represent the continuity of mass and the Navier-Stokes equation for a Newtonian fluid respectively. The computational tool used in this study uses the Navier-Stokes equation to model a fluid control volume. For a solid control volume, the Navier-Stokes equation is not used by the computational solver. Equation (2.3) is the heat energy conservation equation for a fluid control volume. In the absence of a fluid control volume, Equation (2.3) is reduced to the form in Equation (2.4), which describes the heat flow equation in a solid control volume.

Equation (2.5) is the conservation of charge equation in an electrical conductor. This equation is used in modeling the electrical behavior across a solid control volume, as is the case in the thermoelectric unicouples. Equations (2.6) and (2.7) represent the coupled equations of thermoelectricity relating the heat flux across a thermoelectric control volume to an electric potential. For an isotropic thermoelectric control volume, the Seebeck effect, thermal conductivity, and electrical conductivity are represented as single value parameters as opposed to matrix representation.

2.2 Solution Strategy

Modeling the solar thermoelectric generator was performed in four steps. First, was geometry and mesh creation of the STEG unit in the CFD-GEOM environment (Figure 2-1 (a)). Second, the problem type, volume, boundary, and initial conditions were set up using the CFD-ACE solver (Figure 2-1 (b)). Third the post-processing of the numerical solution was performed in the CFD-VIEW environment (Figure 2-1 (c)). Finally, data analysis of the electrical results was performed using MATLAB (Figure 2-1 (d)) to generate power curves.

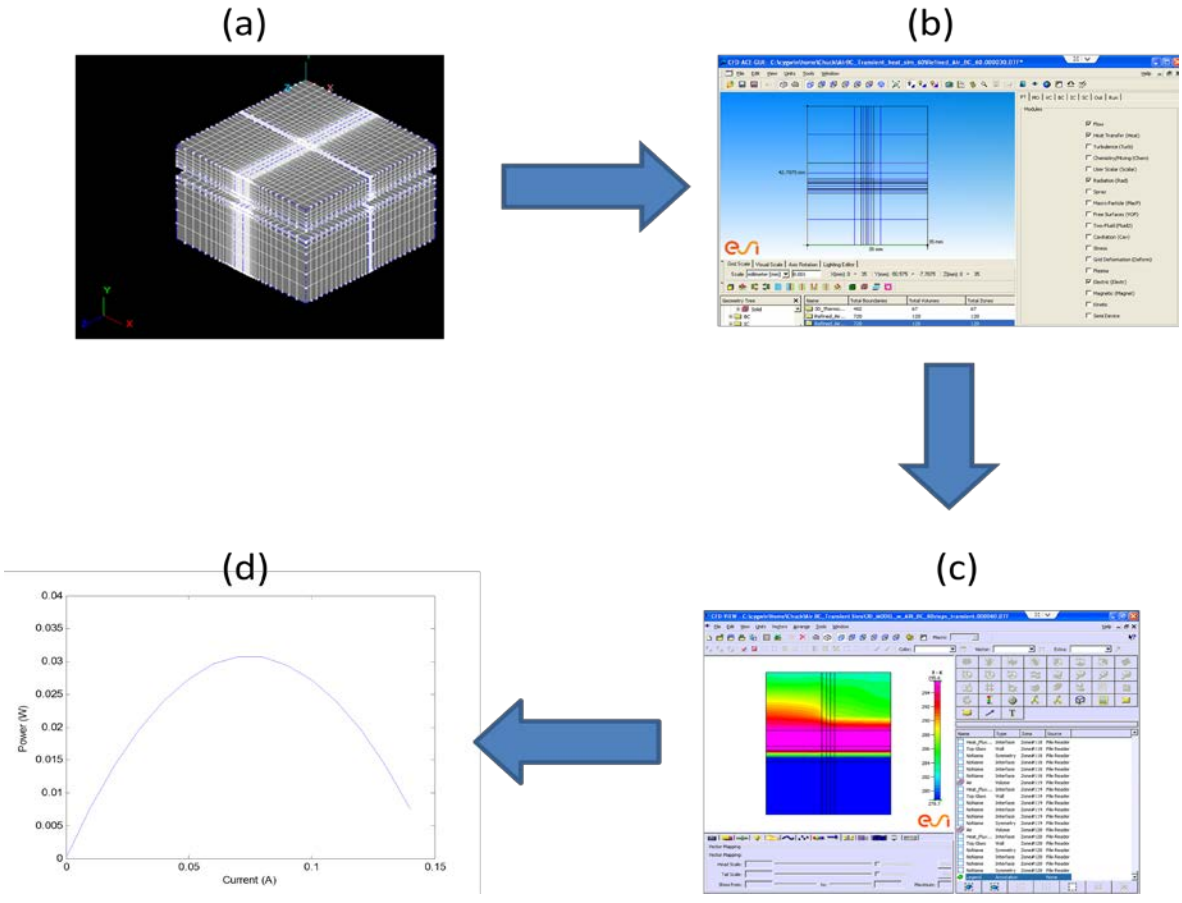

Figure 2-1: Snapshots of (a) CFD - GEOM, (b) CFD - ACE GUI, (c) CFD - VIEW, and (d) MATLAB

2.2.1 Model Geometry

As was described in Chapter 1.2, the computational model STEG was developed using the design information from the experimental study by Sarah Watzman [7]. For comparative purposes, it was imperative to create a computational model that could accurately represent the experimental STEG unit and also be computationally efficient.

Three STEG geometries were created in this study according to the type of simulation to be performed on the respective geometric domain. First, a two-dimensional solid model of the experimental STEG unit was created. Second, a three-dimensional fully solid model was created. Finally, a three-dimensional model consisting of fluid and solid domains was created. A structured mesh was then created for the different geometries.

The two-dimensional solid model was created; closely matching the experimental STEG unit's dimension (absorber plate: 11.5" x 3/16", heat sink: 12" x 5/8") as shown in Figure 2-2.

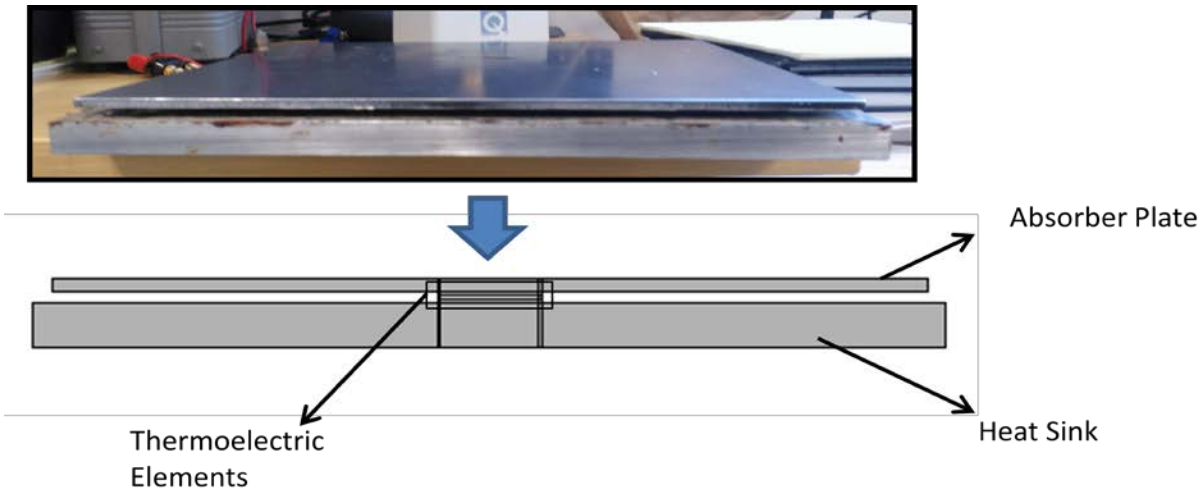

Figure 2-2: 2-D Model of Experimental STEG Unit

The two-dimensional geometry was then meshed using a structured mesh pattern, generating a mesh count of 14,693 cells. This structured mesh can be seen in Figure 2-3.

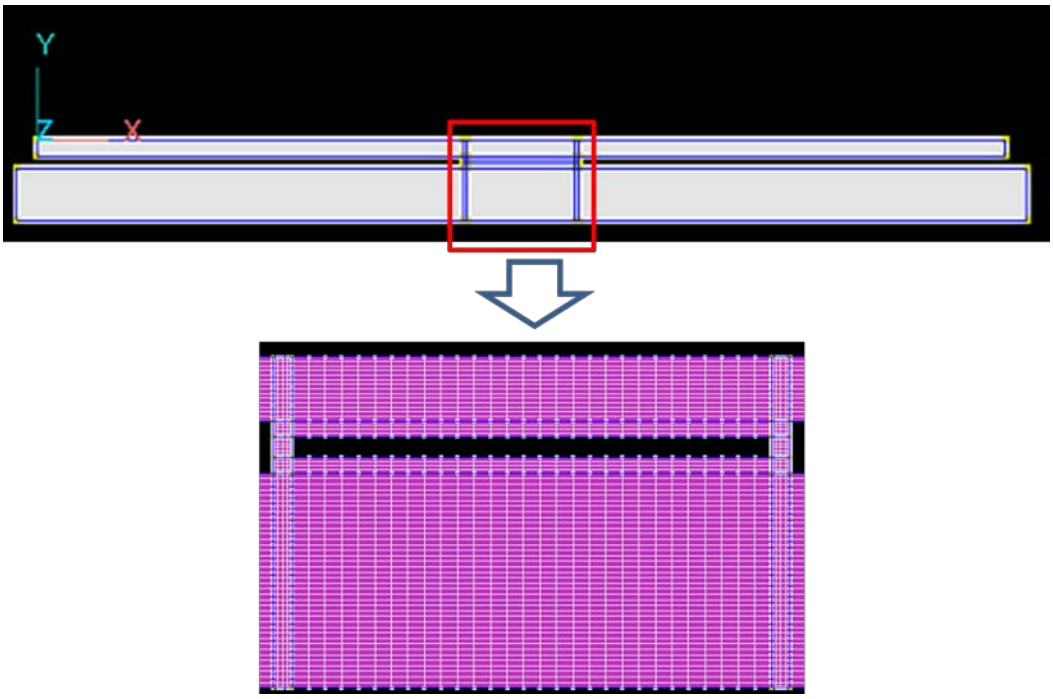

Figure 2-3: Structured Mesh of 2D Geometry

After creating the mesh, the thermal boundaries of the 2-D geometry were chosen as shown in Figure 2-4. For all simulation performed with this geometry, a heat flux was applied to the top of the absorber layer, while the bottom of the heat sink was maintained at an isothermal temperature. The boundary conditions on other sides of the 2-D geometry were varied.

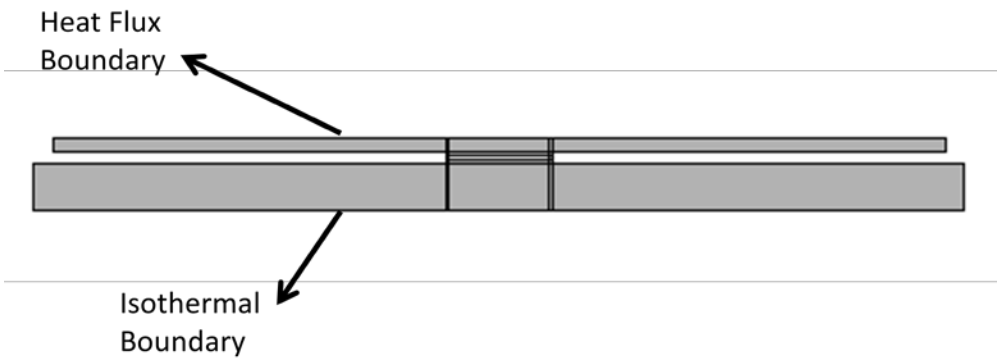

Figure 2-4: Thermal Boundaries of 2-D STEG Model

The computational model was then extended to the third dimension. To reduce the computational cost, the computational domain was scaled down to the size of the thermoelectric module used in the experimental STEG unit, measuring 35 mm x 35 mm. The number of thermoelectric unicouples in the thermoelectric module was also reduced from 126 to 1. Figure 2-5 shows the 3-D solid model developed.

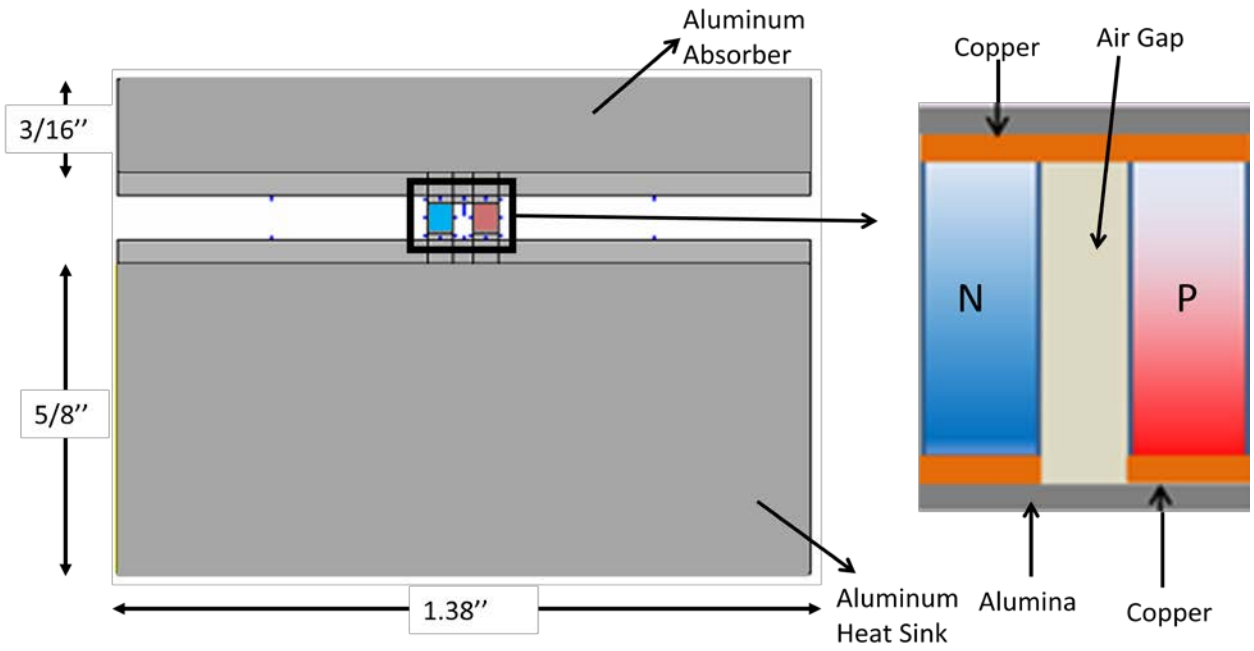

Figure 2-5: 3-D Model Geometry Showing Unicouple

The dimensions of the different components as shown in Figure 2-5 are listed in Table 3 below.

Table 3: Dimension of Model Geometry

3-D Model Components	Dimension [L x W x H] (mm)
Top Plate (Absorber)	35 x 35 x 4.7625
Alumina Layer (top and bottom)	35 x 35 x 1.175
Bottom Plate (Heat Sink)	35 x 35 x 15.875
Thermoelectric Legs	1.29 x 1.29 x 1.5
Copper Layer (top and bottom)	1.29 x 1.29 x 0.4

The thermal boundaries of the three-dimensional model are described in Figure 2-6. Here, a symmetry boundary condition was applied to the external sides of the model which makes the sides adiabatic. This boundary condition was applied because the three-dimensional model only represents an area cut-out by the thermoelectric module. Similar to the two-dimensional case, heat flux and isothermal boundary conditions were applied to the top and bottom surfaces of the three-dimensional solid model respectively. Other surfaces such as the alumina substrate and the thermoelectric legs had varying boundary conditions depending on the simulation type.

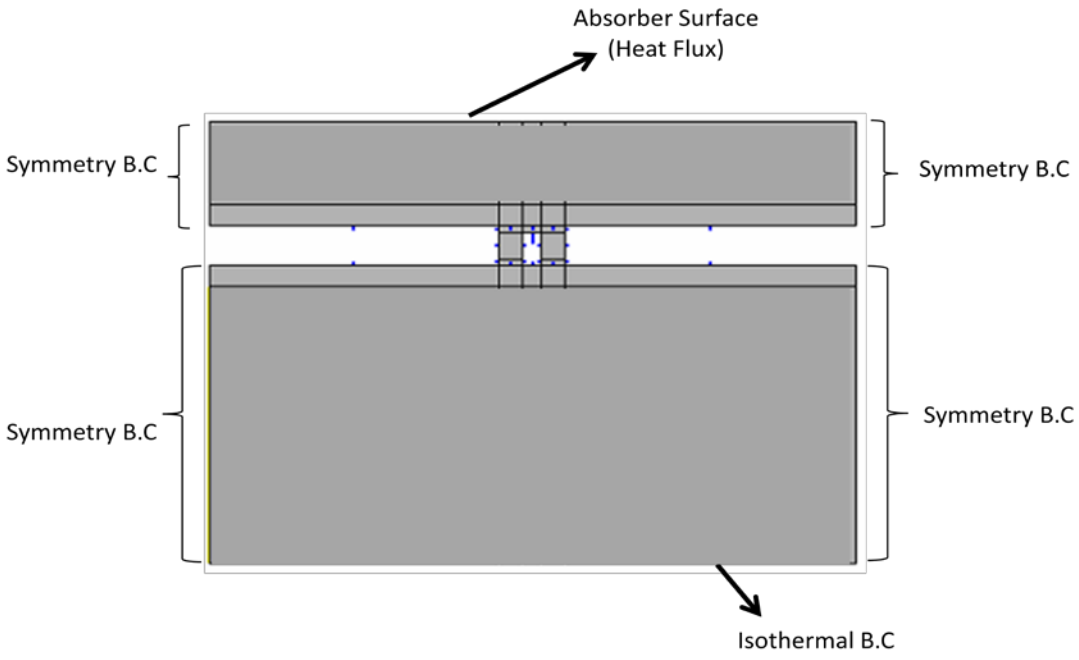

Figure 2-6: Thermal Boundaries of 3-D Model

Figure 2-7 shows the electrical boundaries for the thermoelectric unicouple. The N and P type semiconductors are joined to a copper substrate by a Bismuth-Tin solder. The interface between the semiconductors and the copper substrate was modeled with an electrical contact resistance, as shown. The cross-sectional area of the copper substrate attached to the P-type semiconductor was designated as the positive terminal, from which electric current densities were applied. The other cross-sectional area of the copper substrate as shown was designated as ground, where the electric potential was set to zero.

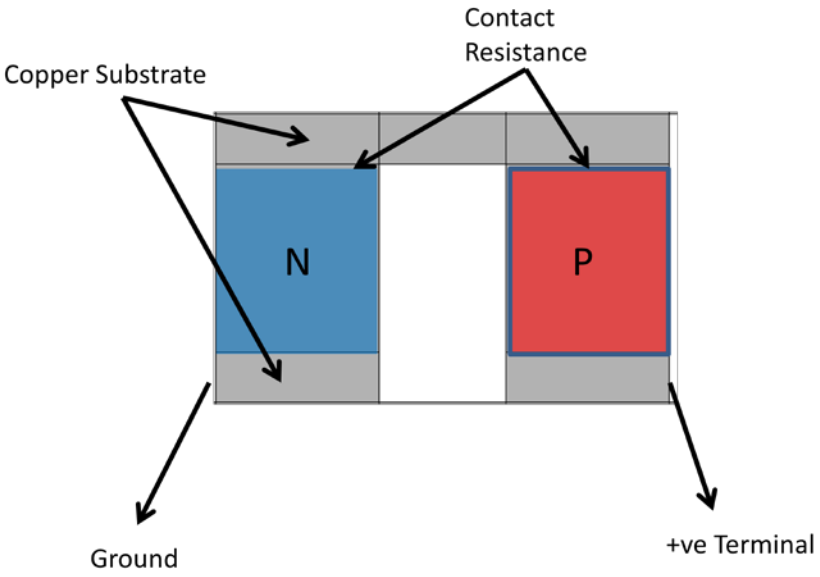

Figure 2-7: Electrical Boundaries of Thermoelectric Unicouple

2.2.2 Three-Dimensional Mesh Creation and Grid Independence Study

To create the three-dimensional geometry and its mesh, a structured grid was created in the top plane as shown in Figure 2-8, and extruded in the z-direction to form the full solid model.

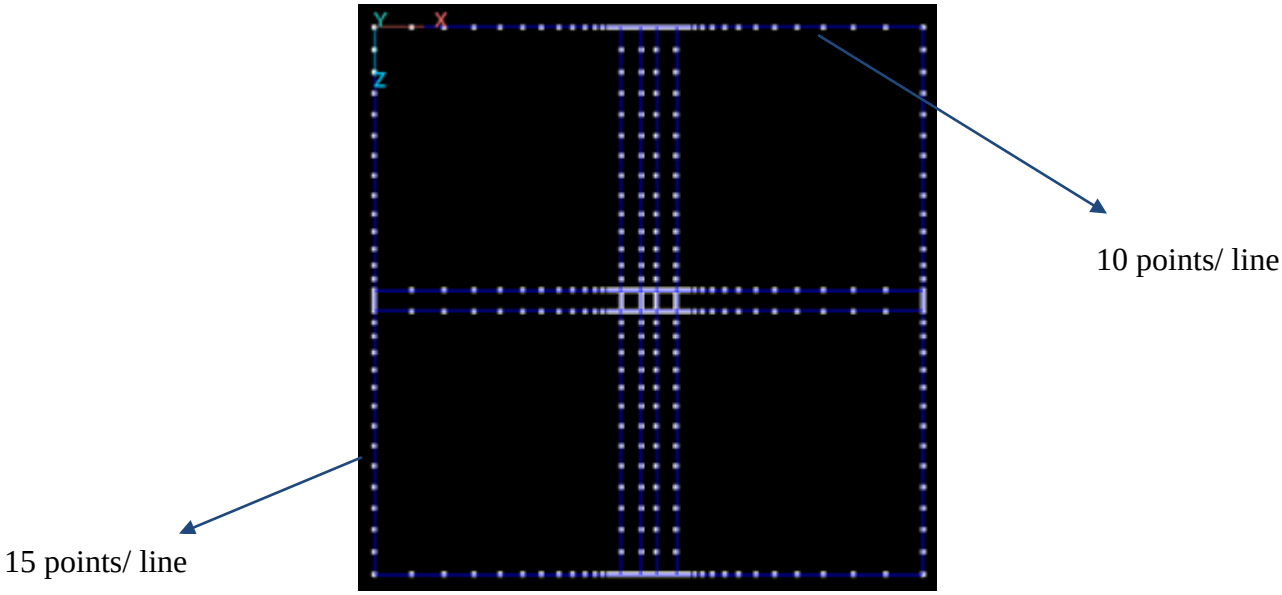

Figure 2-8: Top Plane Showing Grid Points Creation

The grid points on the left/right and top/down edges were created such that they were close to each other approaching the thermoelectric legs at the center. Since the thermoelectric unicouple is the most important component, it was necessary to increase the mesh density in that region.

Figure 2-9 shows a close-up view of the grid points created on the thermoelectric legs.

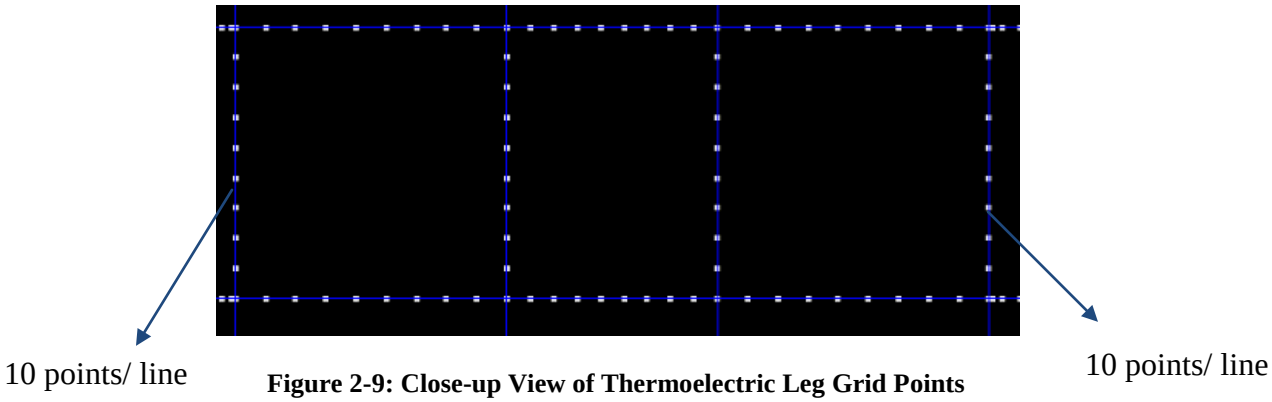

Figure 2-9: Close-up View of Thermoelectric Leg Grid Points

After creating the grid points in the top plane, a structured mesh was formed as shown in Figure 2-10.

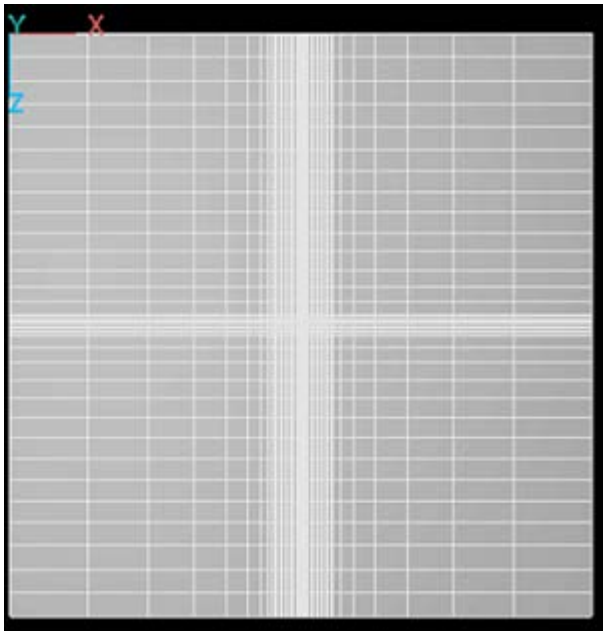

Figure 2-10: Mesh Generated in the Top Plane

From this plane, an extrusion was performed in the Y-direction to create grid points as shown in Figure 2-11 and Figure 2-12.

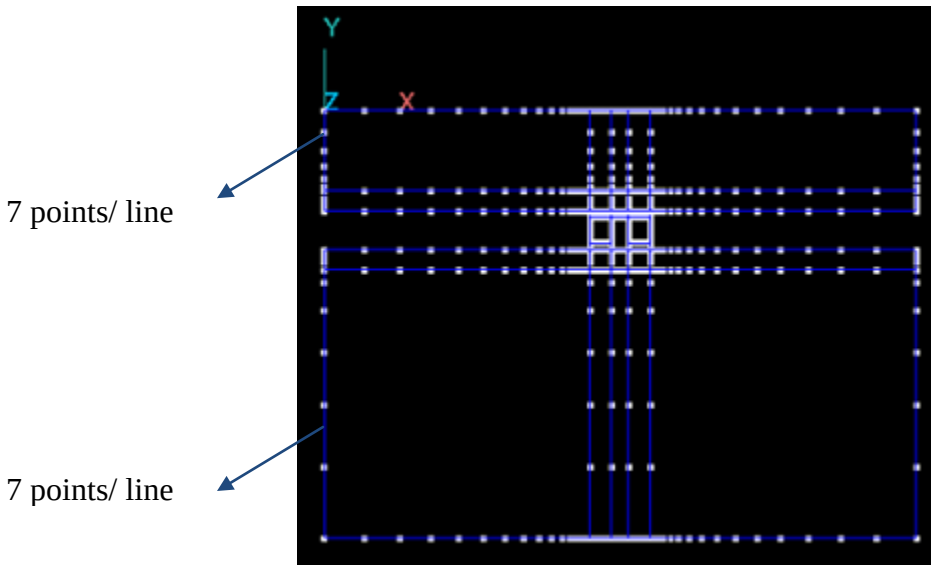

Figure 2-11: Grid Points Generated in the Y-direction

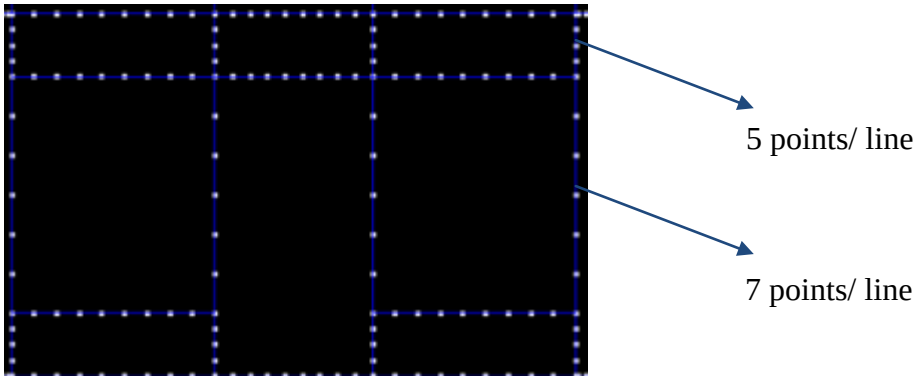

Figure 2-12: Grid Points Generated across Thermoelectric Legs

After establishing a grid pattern for the three-dimensional solid model, a grid independence study was performed to ensure the results were unaffected by the mesh size chosen. In performing this study, a thermal simulation was performed on the three dimensional

model for mesh sizes between 40,000 and 90,000 using the following parameters listed in Table 4 for the boundary conditions in the CFD-ACE solver.

Table 4: Thermal Simulation Parameters for Grid Independence Study

Thermal Boundaries	Boundary Conditions
Top Absorber Surface	1200 W/m^2 heat flux
Bottom of Heat Sink	Isothermal at 300 K
External Sides	Symmetry conditions
Alumina Surface	Radiative and Convective Heat Losses
Ambient Temperature	300 K

The results of the maximum temperature obtained after post processing are summarized in Table 5.

Table 5: Comparative Results of Mesh Convergence Study

Mesh Count (# of Cells)	Maximum Temperature (K)
44,688	435.7
60,902	454.9
72008	454.9
98328	454.9

The results of the mesh convergence study showed that increasing the mesh count beyond 60,900 had no effect on the magnitude of the maximum temperature obtainable. To save computational time, the smaller mesh count of 60,902 was chosen as the final mesh configuration. The final mesh is shown in Figure 2-13.

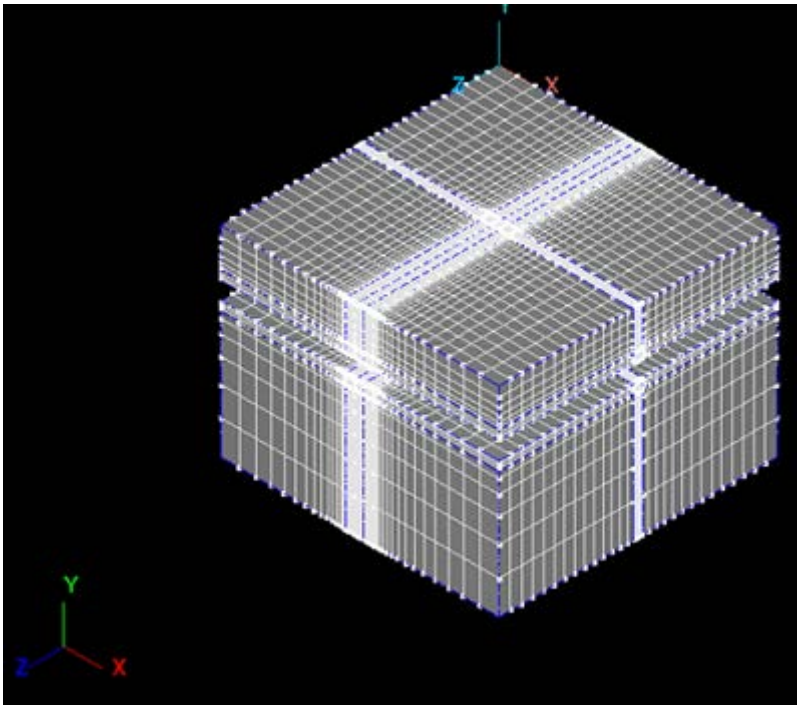

Figure 2-13: Final Mesh Generated for Solid Geometry

The final geometry was created to include a fluid layer interacting with the three dimensional solid model. This geometry was created by extending the mesh at the top of the absorber plate to meet the glass wall as shown in Figure 2-14. The gaps between the solid geometry were closed and meshed to form a second fluid layer.

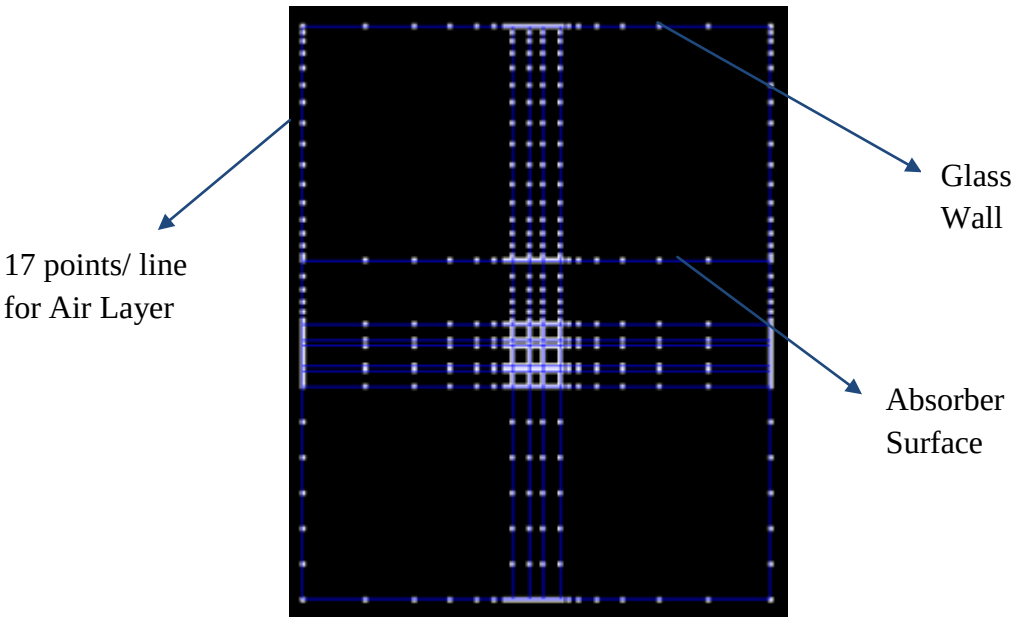

Figure 2-14: Grid Points for Geometry with Air Layers

The final mesh for this geometry is shown in Figure 2-15. The total mesh count for this geometry was 83,250 cells.

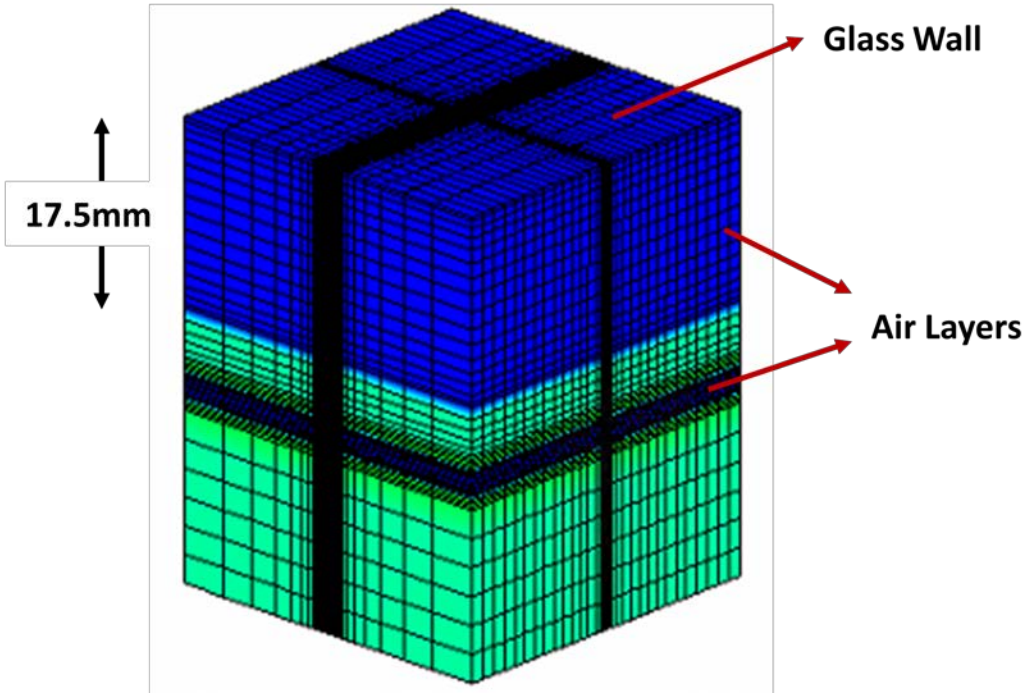

Figure 2-15: 3-D Geometry Mesh with Air Layers

2.2.3 Simulation Set-up and Post Processing

The next step of the solution strategy was performing different simulations with the geometries created in the CFD-ACE solver (Figure 2-16).

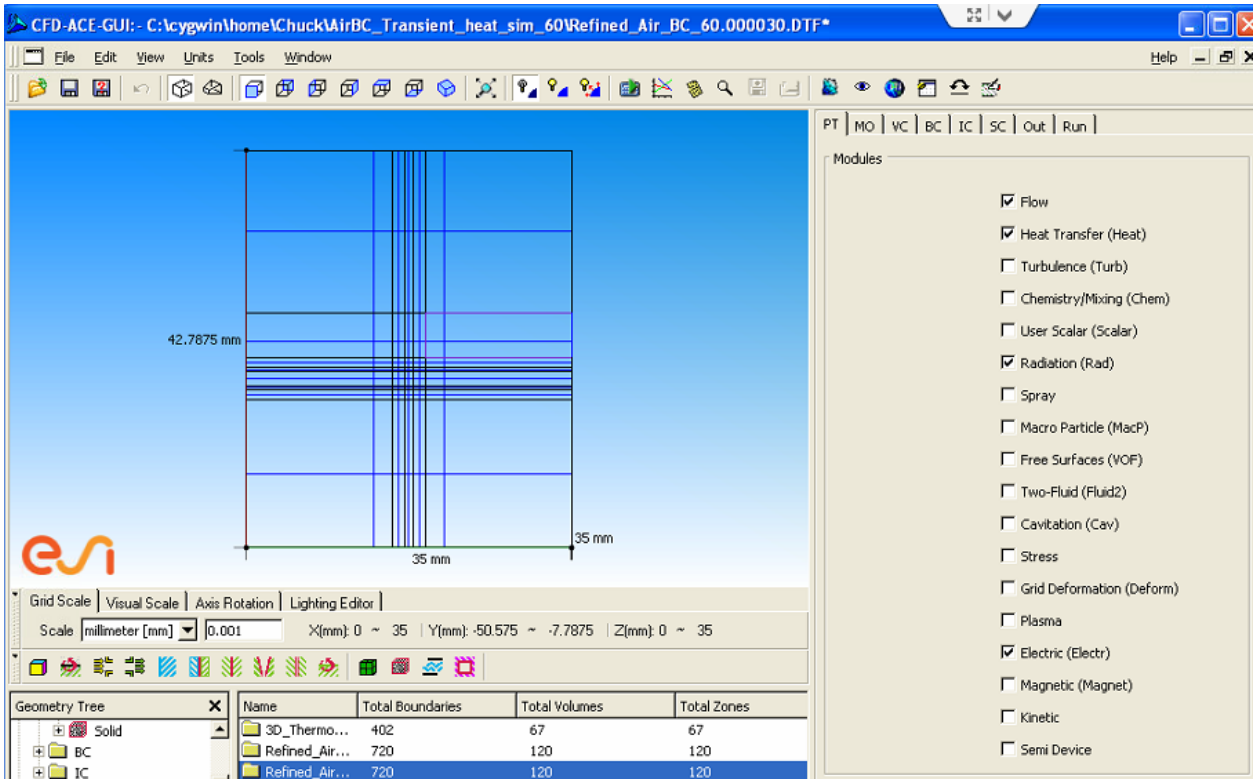

Figure 2-16: CFD-ACE Solver

The sequence of simulations performed in CFD-ACE is shown in Figure 2-17.

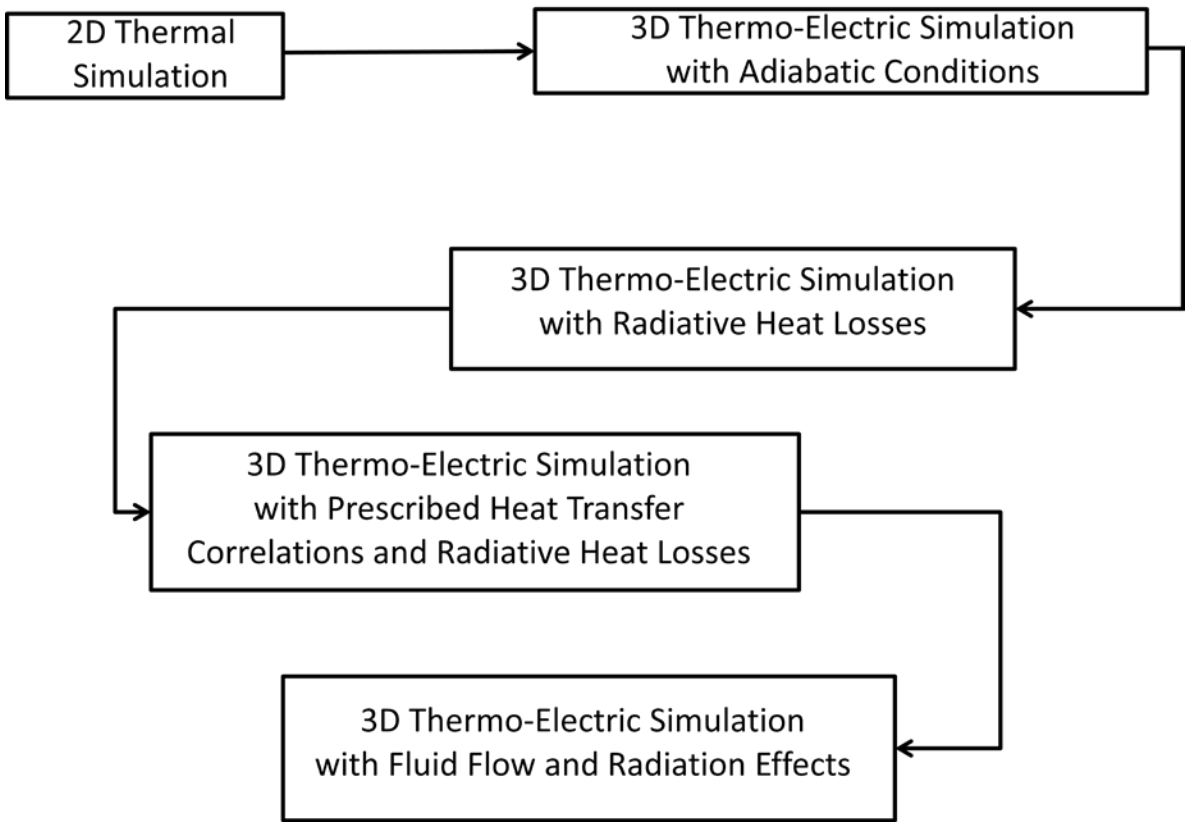

Figure 2-17: Flow Chart Showing the Different Simulations Performed in the CFD-ACE Solver

As shown in Figure 2-17, a thermal simulation was first performed on the two-dimensional STEG model to compare the results to those obtained from hand calculations. Further discussion of this result is discussed in Chapter 3.1. The next three sequences of simulations involved coupled thermal - electric effects and were performed using the three-dimensional solid geometry (Figure 2-13). The last simulation involving fluid flow and radiation effects was performed using the three-dimensional geometry containing fluid layers (Figure 2-15).

Within the CFD-ACE environment, volume conditions/material properties were set for each model component as listed in Table 6 [10]. This volume conditions were the same for the different model geometries created, except in the case of an air layer for the geometry in Figure 2-15.

Table 6: Values of Material Properties used in Solver

Material Type	Property	Value
Alumina	Density ρ	3720 kg/m^3
	Specific Heat c_p	880 J/kg-K
	Thermal Conductivity k	25 W/m-K
	Electrical Conductivity σ	Non conductor
Aluminum	Density ρ	2702 kg/m^3
	Specific Heat c_p	903 J/kg-K
	Thermal Conductivity k	240 W/m-K
	Electrical Conductivity σ	Non conductor
Copper	Density ρ	9813 kg/m^3
	Specific Heat c_p	385 J/kg-K
	Thermal Conductivity k	401 W/m-K
	Electrical Conductivity σ	5.96 x 10^7 (Ω-m)$^{-1}$
Bismuth-Telluride P-type	Density ρ	7700 kg/m^3
	Specific Heat c_p	544 J/kg-K
	Thermal Conductivity k	1.2 W/m-K
	Electrical Conductivity σ	4.762 x 10^4 (Ω-m)$^{-1}$
	Seebeck Coefficient S	225 x 10^{-6} V/K
Bismuth-Telluride N-type	Density ρ	7700 kg/m^3
	Specific Heat c_p	544 J/kg-K
	Thermal Conductivity k	1.2 W/m-K
	Electrical Conductivity σ	3.703 x 10^4 (Ω-m)$^{-1}$
	Seebeck Coefficient S	-230 x 10^{-6} V/K
Air	Molecular Weight	29 kg/kmol
	Dynamic Viscosity	1.7505 x 10^{-5} kg/m-s
	Specific Heat (at 278.7 K)	1005.7 J/kg-K
	Thermal Conductivity k	0.0245 W/m-K
	Electrical Conductivity	Non conductor

The boundary conditions for heat flux, fluid velocity, mode of heat transfer, current density, electric potential, emissivity, spectral refractive index, and absorption coefficient were

set depending on the type of simulation being investigated. Further discussion of this can be found in Chapter 3. After all parameters were entered, the simulations were set to be solved for a convergence criterion of 0.0001. As the solution progressed, a residual plot was generated to capture the solutions convergence behavior. A sample residual plot is shown in Figure 2-18.

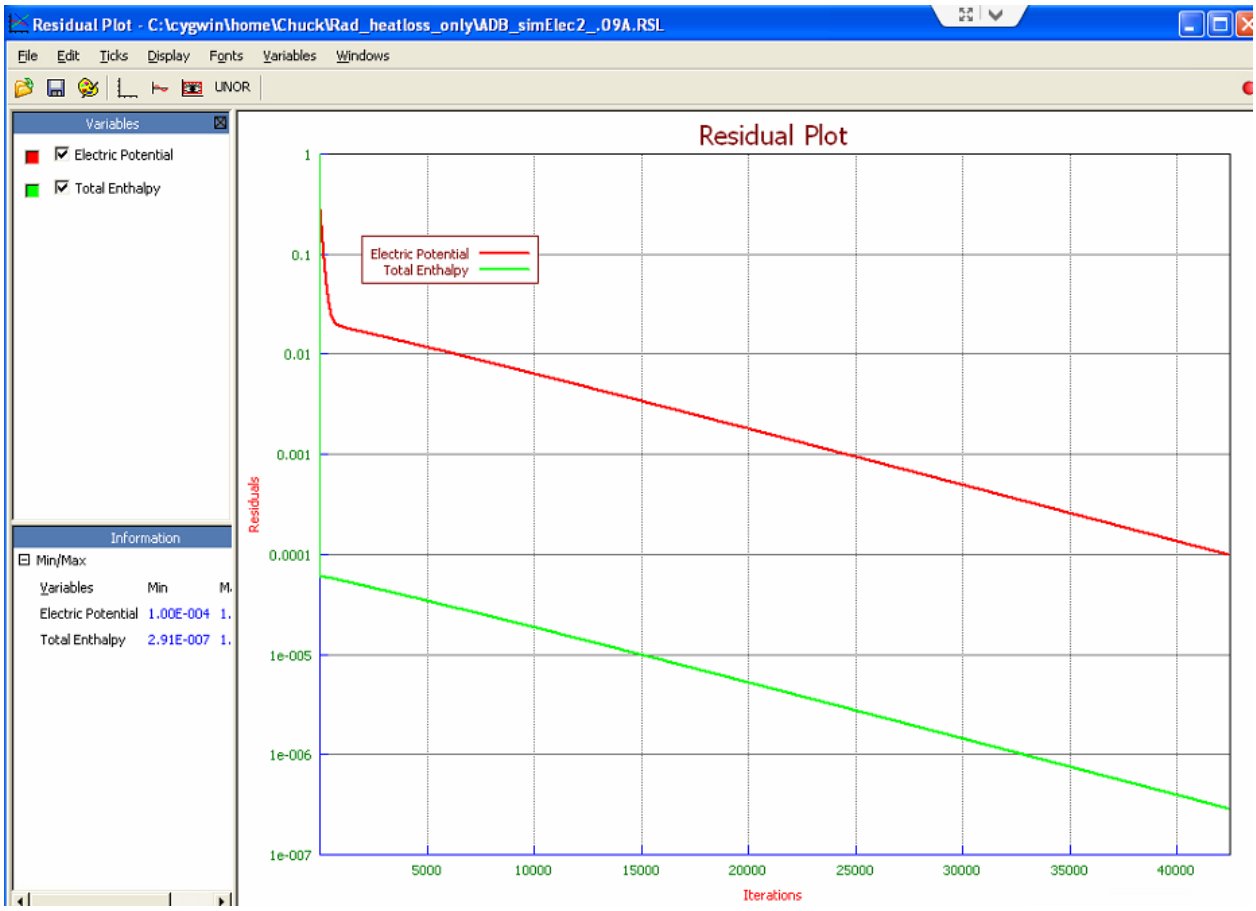

Figure 2-18: Sample Normalized Residual Plot with a 0.0001 Convergence Criteria

The post processing of the numerical solutions was performed in CFD-VIEW. The primary results investigated in the post-processing were the temperature distribution and the voltage distribution as shown in the CFD-VIEW images in Figure 2-19 and Figure 2-20 respectively.

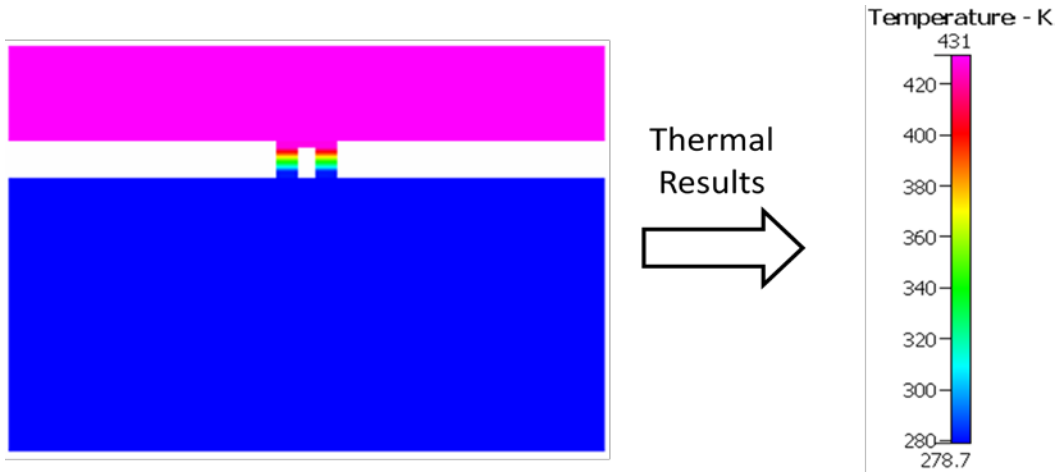

Figure 2-19: Sample CFD-VIEW Image of Temperature Distribution

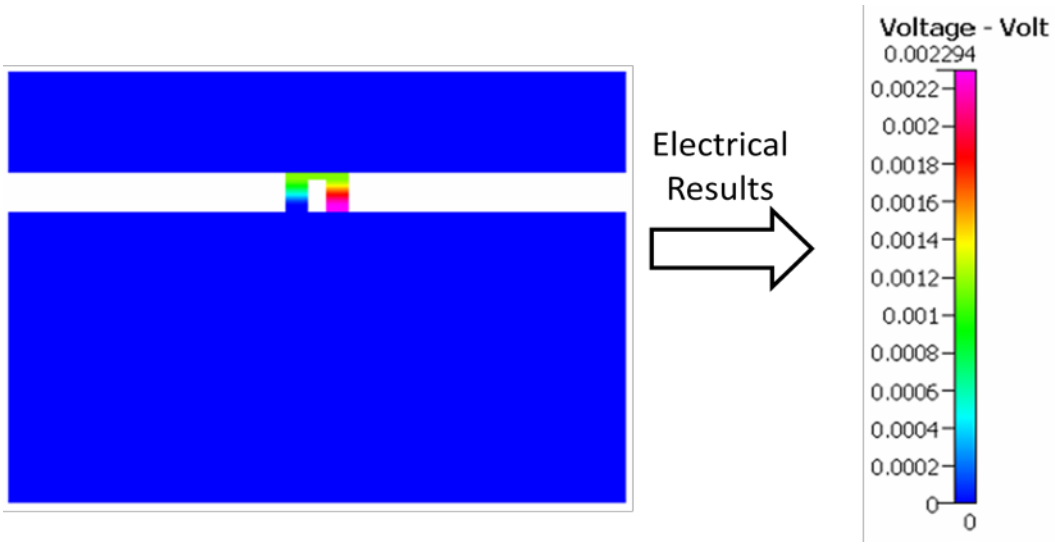

Figure 2-20: Sample CFD-VIEW Image of Voltage Distribution

The numerical results of different electrical boundary conditions for each simulation type were then analyzed using MATLAB software. Here, power curves were generated and compared for the different simulations. A sample MATLAB power curve is shown in Figure 2-21.

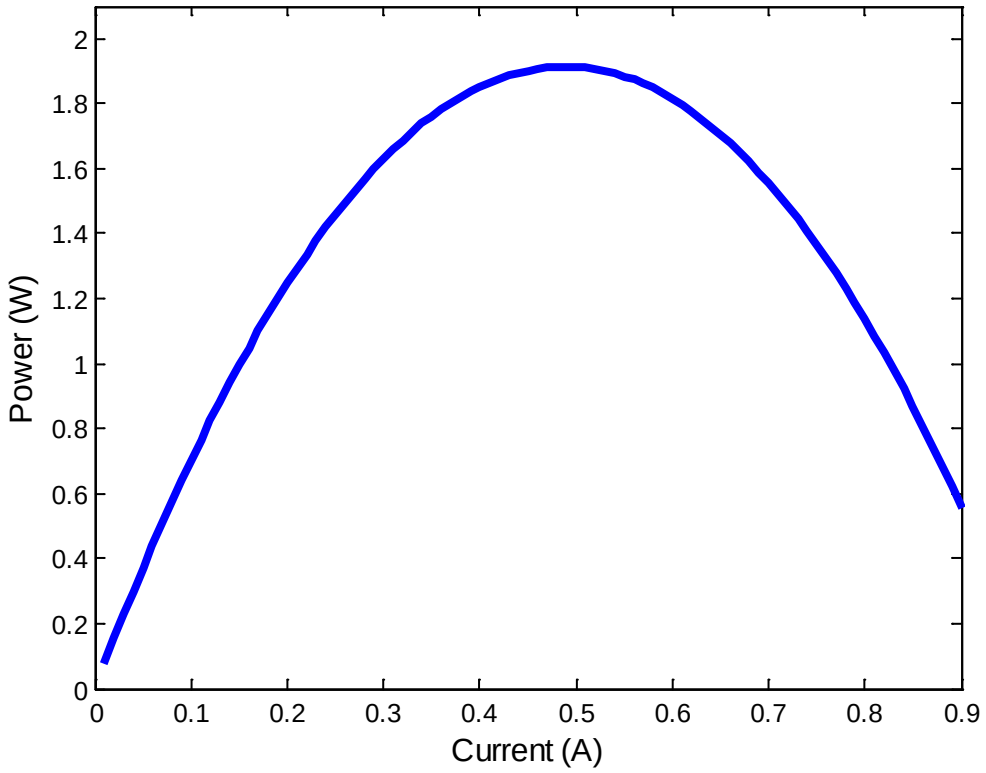

Figure 2-21: Sample Power Curve Generated in MATLAB

Chapter 3
Results and Discussions

The results of this study are presented in the order in which the simulations were performed, as described in Chapter 2.2.3.

3.1 Simulations with Two-Dimensional Geometry – Verification Study

A steady state thermal simulation was performed using the two-dimensional model, involving a heat flux of 1200 W/m^2 on the absorber surface, and an isothermal boundary condition at the bottom of the heat sink. All other boundaries were assumed to be adiabatic. The result of the numerical solution is shown in Figure 3-1.

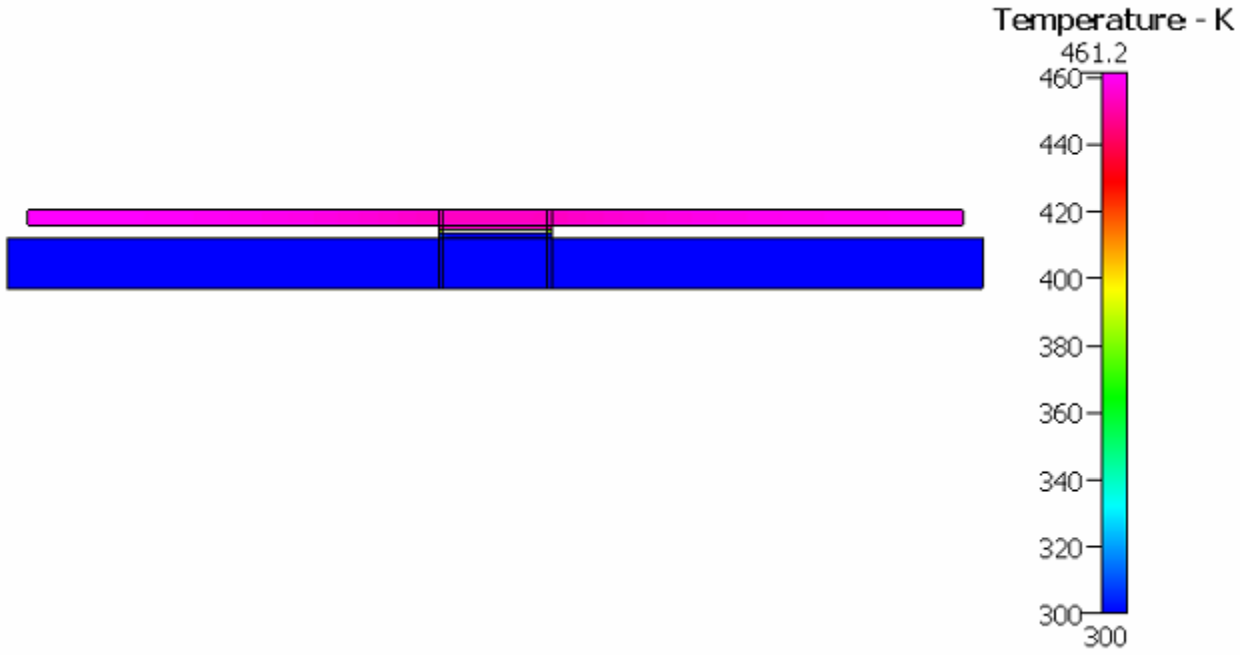

Figure 3-1: Thermal Simulation Results for 2-D Model

The numerical results were verified by performing a lumped parameter analysis for the heat transfer through the absorber plate. The equations used for this calculation are described below;

$$Q_{absorber-2D} = \ q"_{in}.A_{absorber-2D} = \frac{2.k.A_{leg\_2D}}{L_{leg}} \ (T_{max} - \ T_{amb}) \qquad (3.1)$$

Where $Q_{absorber-2D}$ is the net heat rate applied to the absorber plate, $q"_{in}$ is the input heat flux, $A_{absorber-2D}$ is two-dimensional area of the absorber plate, k is the average thermal conductivity of the two thermoelectric legs, A_{leg_2D} is the two-dimensional cross-sectional area of the thermoelectric legs, L_{leg} is the height of each thermoelectric leg, T_{max} is the maximum absolute temperature obtained at steady state, T_{amb} is the absolute ambient temperature.

A maximum temperature of 456.7 K was obtained for the hand calculation, which was within 1% of the numerical solution. With this result, the numerical solver was verified.

3.2 Simulations with Adiabatic Conditions

A coupled thermal-electric simulation was performed using the three dimensional solid model under adiabatic conditions. The result of this simulation represents the upper limit of the STEG performance, as the maximum temperature gradient is achieved under adiabatic conditions of operation. The assumptions made for this simulation are presented as follows;

- The simulation was performed at steady state
- The ambient temperature was assumed to be the same as the estimated experimental temperature at 278.7 K

- The bottom of the heat sink was assumed to be isothermal at 278.7 K
- The electrical conductivity of all components was assumed to be zero except those of the thermoelectric legs and the copper substrate.
- An electrical contact resistivity at 10% of the resistivity of the Bismuth-Telluride legs (2.7632×10^{-7} Ω.m) was used at the interfaces of the copper substrate and the semiconductors.
- The net voltage obtained from the thermoelectric module was assumed to be equivalent to that obtained by multiplying the voltage produced in the unicouple by 126 unicouples.

A heat flux of 406 W/m^2 was applied to the top of the absorber surface. This heat flux was obtained by multiplying together the parameters in Table 7. No heat loss was allowed at the top surface of the absorber plate. Adiabatic boundary conditions were applied to all other surfaces, except the bottom of the heat sink which was isothermal.

Table 7: Parameters Used to Calculate the Applied Heat Flux in Adiabatic Simulation

Measured solar flux (average of experimental) [7]	792 W/m^2
Transmissivity of soda-lime glass	0.9
Emissivity of solar coating on absorber plate	0.9
Estimated cosine of solar zenith angle at mid-day for latitude 40 °N in the month of March (NOAA Database)	0.6328

The thermal result of the coupled thermal-electric simulation is shown in Figure 3-2. Here a maximum temperature of 150.3 K was produced across the thermoelectric legs.

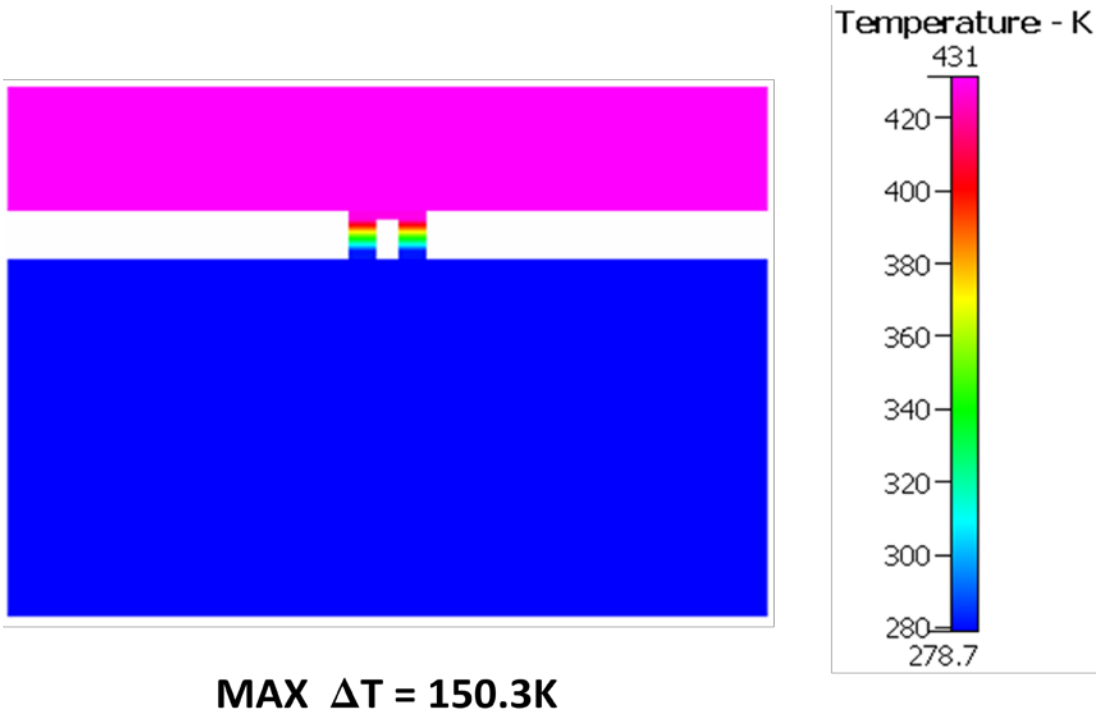

Figure 3-2: Temperature Distribution for Adiabatic Simulation

3.2.1 Electrical Simulation Result for Adiabatic Conditions.

The electrical simulation was performed over a range of current from 0.0005 A - 0.9 A. The temperature gradient across the thermoelectric legs remained relatively constant over this range of current. Figure 3-3 shows the power curve of the adiabatic simulation over a range of different currents. Here a peak module voltage and power of 7.78 V and 1.78 W were produced respectively.

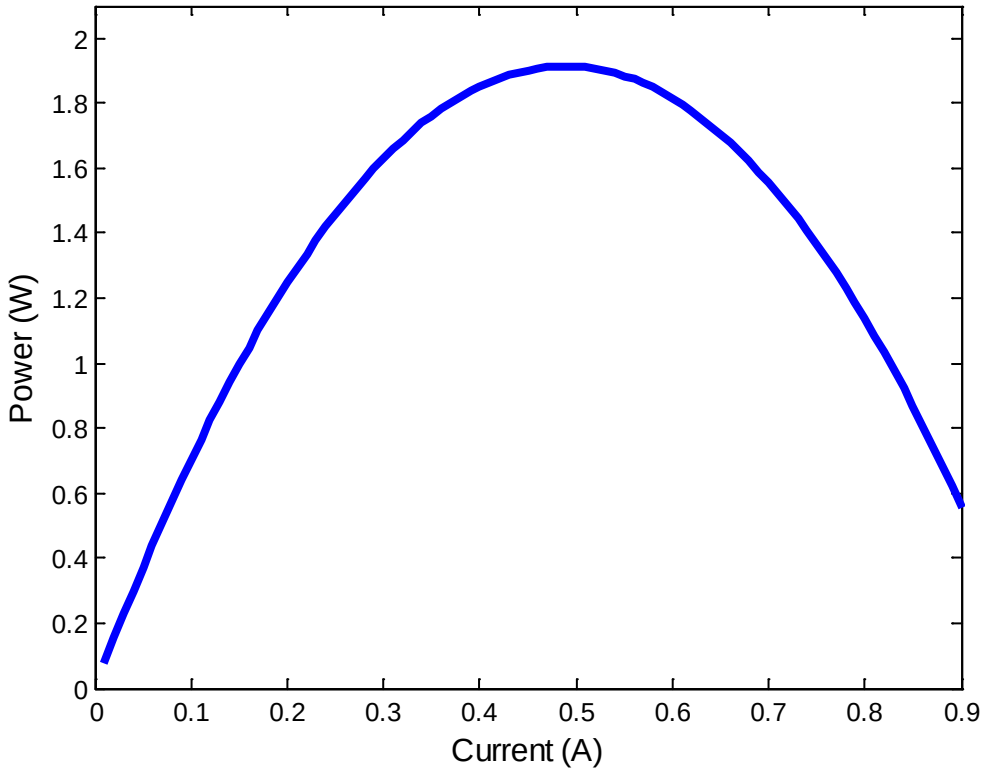

Figure 3-3: Power Curve for Adiabatic Simulation

3.3 Simulations with Radiative Losses Alone

The next simulation performed was a steady state thermo-electric simulation to investigate the effects of heat losses by radiation alone on the performance of the STEG unit, as is the case if the STEG unit is operated in vacuum. The assumptions and boundary conditions for this simulation were similar to those in section 3.2 for the adiabatic case, except the application of boundary conditions of heat losses by radiation from surfaces with prescribed emissivities (Table 8). These surfaces were the alumina layers and the surfaces of the thermoelectric legs Figure 3-4.

Table 8: Emissivity Values Used in Radiative Simulation

Model Surface	Emissivity
Alumina (white 96%)	0.039
P-type Bismuth Telluride	0.45
N-type Bismuth Telluride	0.45

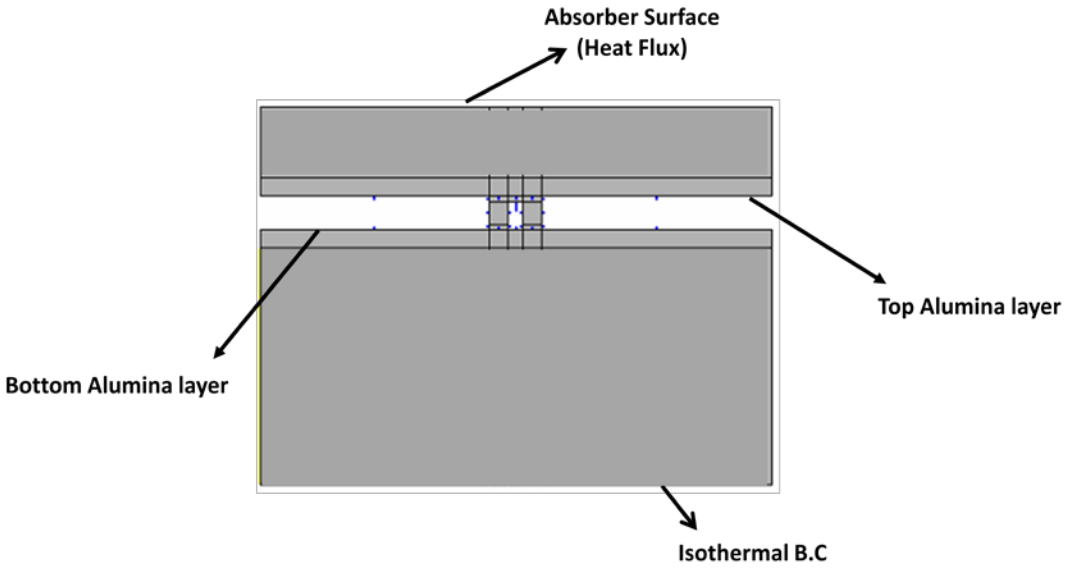

Figure 3-4: Thermal Boundaries of 3-D Model

The simulation was then solved for a convergence criterion of 1×10^{-7}. The residual plot for the heat transfer simulation can be seen in Figure 3-5.

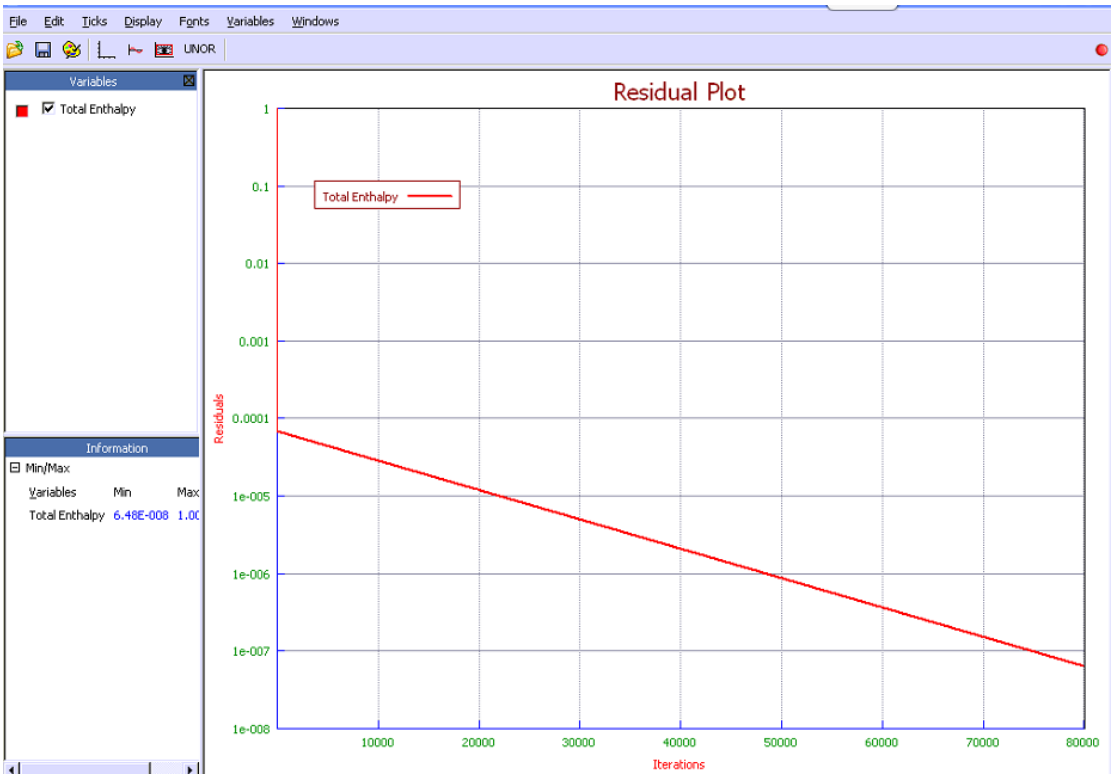

Figure 3-5: Residual Plot of Radiative Heat Loss Simulation

The temperature distribution obtained for this simulation is shown in Figure 3-6.

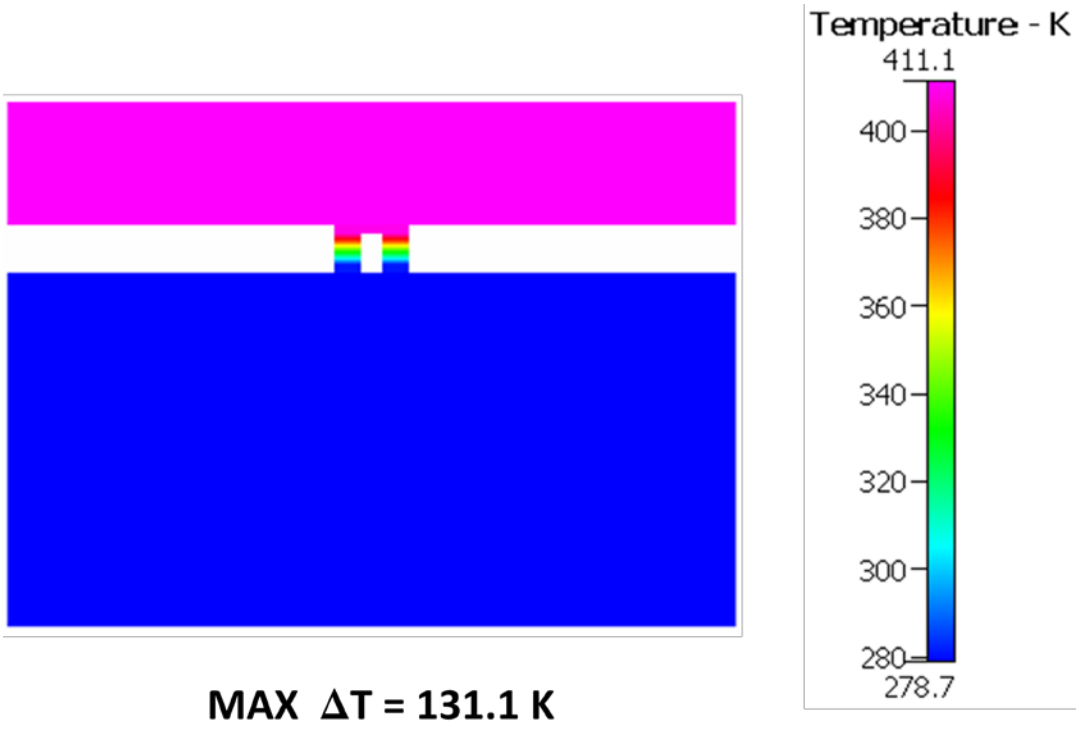

Figure 3-6: Temperature Distribution with Radiative Heat Losses Alone

Here, a maximum temperature gradient of 131.1 K was obtained across the thermoelectric legs. This temperature gradient is 12.7% less than that obtained under adiabatic conditions.

3.3.1 Electrical Simulation Result for Radiative Heat Losses Alone.

Figure 3-7 shows the power vs. current curve for this simulation. A peak voltage and power of 6.52 V and 1.43 W were produced respectively.

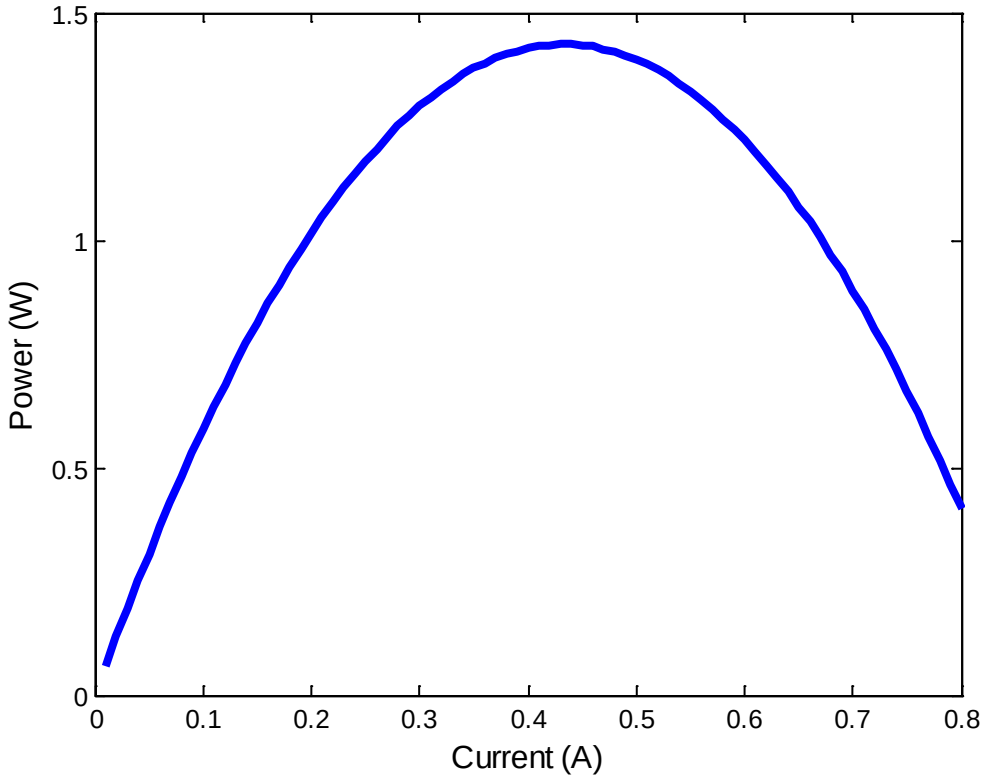

Figure 3-7: Power Curves for Radiative Heat Losses Alone

The power curves of the radiative and adiabatic simulations are shown in Figure 3-8. The peak power produced in the radiative simulation is 19.7% less than the peak power obtained under adiabatic conditions.

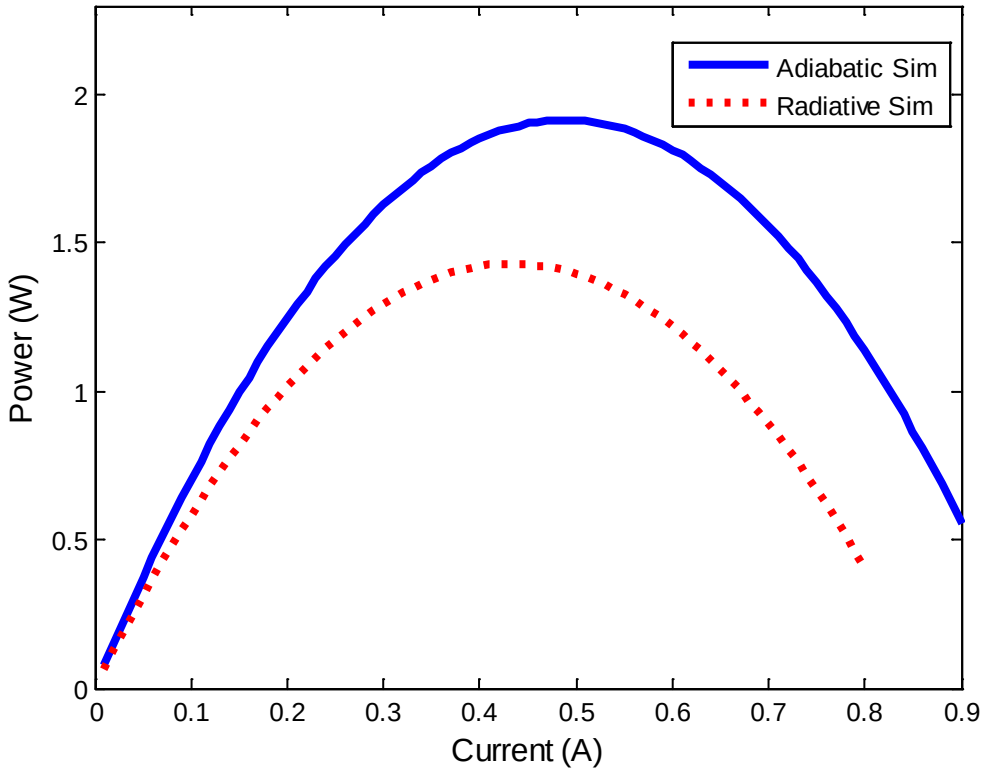

Figure 3-8: Plots Comparing Adiabatic and Radiative Heat Loss Simulation

3.4 Simulations with Heat Transfer Coefficients and Radiative Losses

To model the effects of heat losses by natural convection, a steady state simulation was performed using the three-dimensional solid model. Prescribed heat transfer correlations for natural convection were calculated for the top of the absorber surface and the alumina layers Figure 3-4.

The heat transfer coefficient at the top of the absorber plate was calculated using the natural convection correlation for the upper surface of a horizontal hot plate Equation 3.4.1 [10];

$$\overline{Nu}_L = 0.54\, Ra_L^{\frac{1}{4}} \qquad (10^4 \leq Ra_L \leq 10^7, \text{Pr} \geq 0.7) \tag{3.4.1}$$

$$Ra_L = \frac{g\beta(T - T_\infty)L^3}{\alpha\nu} \tag{3.4.2}$$

$$L = \frac{A_{absorber\_model}}{P} \tag{3.4.3}$$

Where $\overline{Nu}_L$ is the Nusselt number, Ra_L is the Rayleigh number calculated over a characteristic length, Pr is the Prandtl number of the fluid (air), g is the acceleration due to gravity, β is the thermal expansion coefficient of the fluid (air), T is the absolute temperature of the prescribed surface, T_∞ is the ambient temperature, L is the characteristic length calculated for the three-dimensional model, α is the thermal diffusivity of air, ν is the kinematic viscosity of air, and P is the perimeter of the absorber plate used in the three-dimensional model.

The heat transfer coefficient for the top alumina layer was calculated using the natural convection correlation for the lower surface of a horizontal hot plate [10]

$$\overline{Nu}_L = 0.54\, Ra_L^{\frac{1}{5}} \qquad (10^4 \leq Ra_L \leq 10^7, \text{Pr} \geq 0.7) \tag{3.4.3}$$

The heat transfer coefficient for the bottom alumina layer was calculated using the natural convection correlation for the upper surface of a horizontal cold plate which is the same as Equation 3.4.3.

In calculating the heat transfer correlations, the temperature T of each surface under investigation, was estimated apriori and used in estimating the heat transfer coefficient in Equations 3.4.1 - 3.4.3, to be prescribed on the applicable surface. The process was repeated iteratively until the estimated temperature in the calculation matched the temperature produced

by CFD-ACE for each prescribed heat transfer coefficient applied to one surface at a time. Since the CFD-ACE Solver could not apply a thermal heat flux and prescribed heat loss on the same boundary, the calculated heat transfer coefficients for the top absorber plate and the top alumina layers were added and applied to the top alumina layer. By so doing, an approximate value of the heat losses by convection from the top surface could be found. Prescribed radiative effects as in the case of section 3.3 were also simulated

The electrical boundary conditions and assumptions were the same as in the simulation for adiabatic conditions and the simulation with radiative heat loss. The coupled thermo-electric effects were solved for a convergence criterion of 1×10^{-6} as shown in Figure 3-9.

Figure 3-9: Residual Plot for Simulation with Prescribed Heat Transfer Coefficients

The thermal result of this simulation is shown in Figure 3-10. Here a maximum temperature of 19.5 K was produced across the thermoelectric legs.

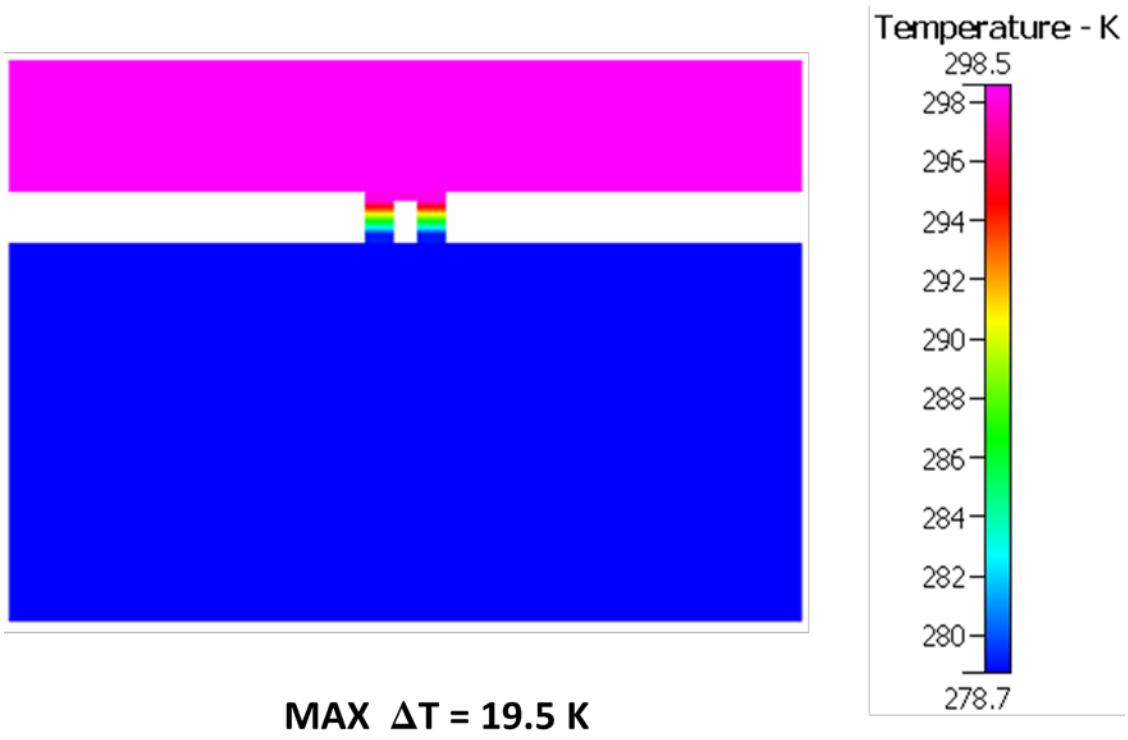

Figure 3-10: Temperature Distribution for Simulation with Heat Transfer Coefficients

3.4.1 Electrical Simulation Result for Convective and Radiative Heat Losses

The electrical simulation was performed for currents in the range of 0.01 A – 0.15 A. The voltage distribution across the unicouple at the maximum power corresponding to 0.09 A is shown in Figure 3-11. The voltage produced by the unicouple at the maximum power was 0.003371 V. Figure 3-12 shows the scaled power curve for the thermoelectric module over the stated range of currents. A maximum power of 0.0385 W was produced.

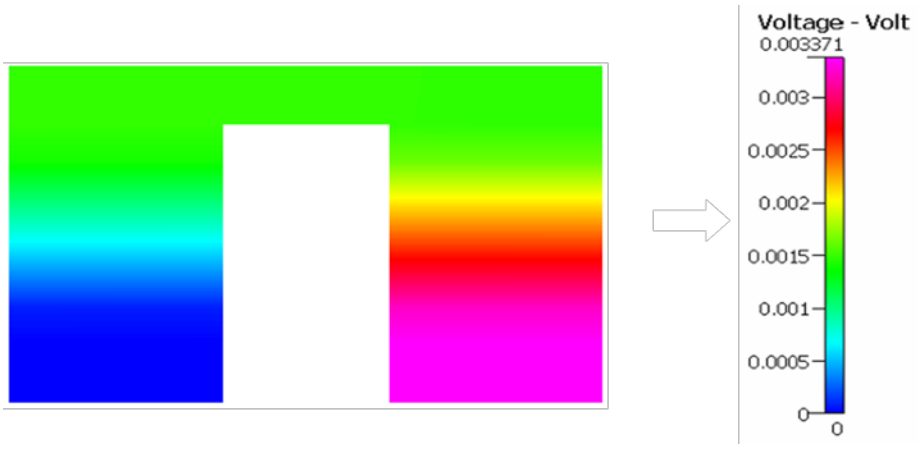

Figure 3-11: Voltage Distribution across Unicouple at Maximum Module Power

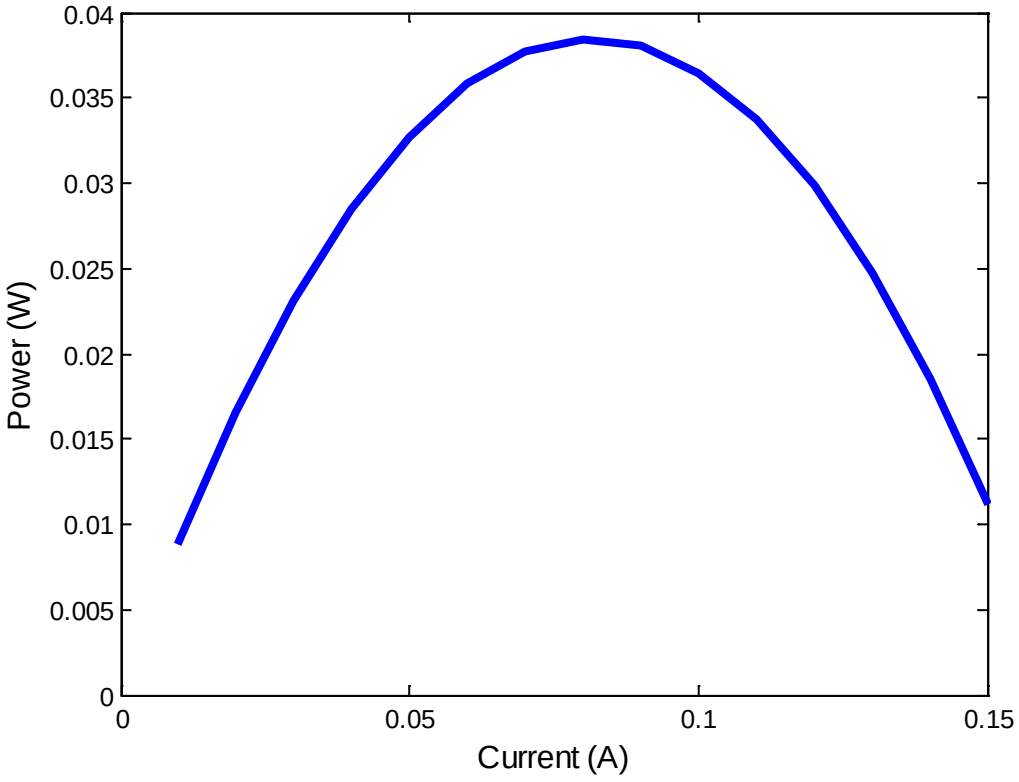

Figure 3-12: Power Curve for Simulation with Convection Coefficients

3.5 Simulation with Fully Coupled Effects

Using the model geometry with a fluid layer, a transient based simulation with the effects of fluid flow, heat transfer, and radiation was performed using a time step of 60 for 60 seconds each. Unique output files were created after the solution of each time step was complete. The volume conditions in this simulation were the same as described in Table 6. A description of the important boundary surfaces for this simulation is shown in Figure 3-13. Only at this surfaces are boundary conditions specified. Symmetry boundary conditions were applied to all external side surfaces of the geometric model.

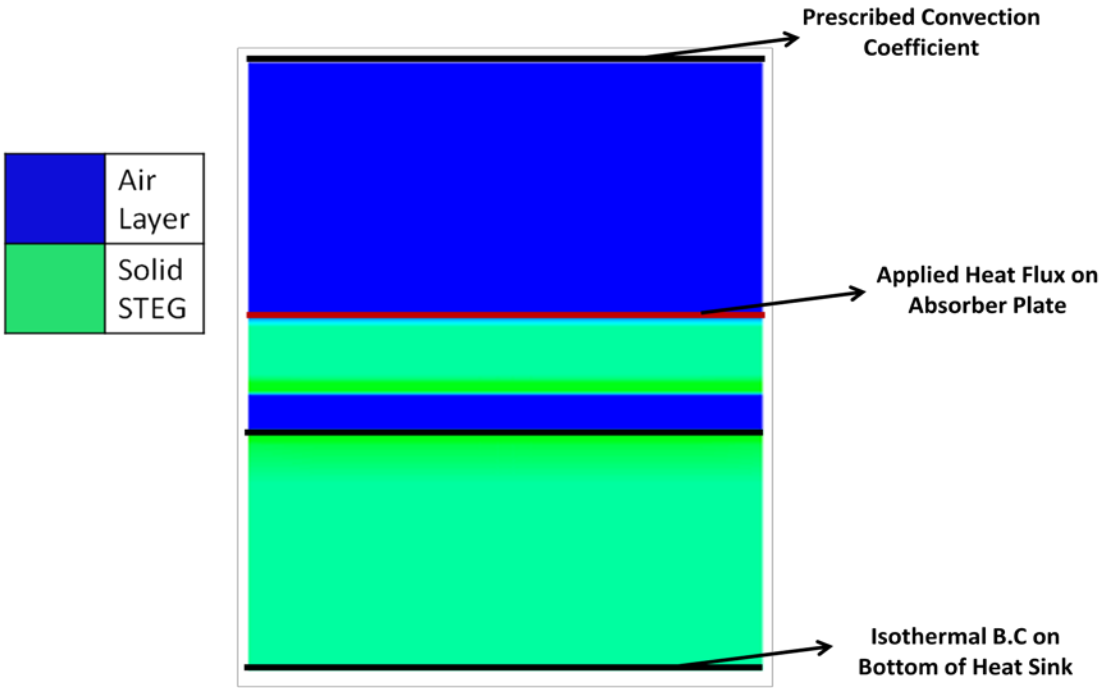

Figure 3-13: Boundary Conditions on Fully Coupled Model

The radiative properties of the surfaces for this simulation are presented in Table 9. The radiation effects in this model were different from those discussed in the other simulation, which were prescribed radiation heat losses computed using the emissivity of the surface and the ambient temperature. Radiation heat transfers between interacting surfaces, in the previous simulations, were not accounted for. In this simulation however, radiation heat transfer between the surfaces in the model is taken into full consideration.

Table 9: Radiative Properties of Surfaces

Surface	Properties	Values in CFD-ACE+™
Glass Layer	Absorption Coefficient	Transparent: -1
	Emissivity	0.1
	Spectral Refractive Index	1
	Specularity	Diffusive: 0
Alumina Layer	Absorption Coefficient	Opaque: 0
	Emissivity	0.039
	Spectral Refractive Index	1
	Specularity	0.5
Thermoelectric Legs	Absorption Coefficient	Opaque: 0
	Emissivity	0.45
	Spectral Refractive Index	1
	Specularity	0.5
Absorber Surface	Absorption Coefficient	Opaque: 0
	Emissivity	0.9
	Spectral Refractive Index	1
	Specularity	Diffusive: 0
Heat Sink Bottom	Absorption Coefficient	Opaque: 0
	Emissivity	0.1
	Spectral Refractive Index	1
	Specularity	Diffusive: 0
Copper	Absorption Coefficient	Opaque: 0
	Emissivity	0.03
	Spectral Refractive Index	1
	Specularity	0.5

3.5.1 Input Parameters on Boundary Surfaces

On the absorber plate, a heat flux of 451.11 W/m^2 was applied. This value was estimated based on the solar heat flux measured from the experimental study, the transmissivity of soda-lime glass, and the cosine of the solar zenith angle for latitude 40 °N at which the experiment was performed in the Month of March. These values are summarized in Table 10. The parameters in Table 10 were multiplied to give a net heat flux of 451.11 W/m^2. Since radiative heat losses are allowed to occur from the top of the absorber plate a different heat flux was used.

Table 10: Parameters used to Estimate Input Heat Flux for Fully Coupled Model

Measured solar flux (average) [7]	792 W/m^2
Transmissivity of soda-lime glass	0.9
Cosine of solar zenith angle	0.6329

The bottom of the heat sink was modeled as an isothermal surface. This surface was maintained at 278.7 K, which was the estimated ambient temperature under which the experiment was performed. On the glass wall, a convective heat transfer coefficient was calculated using the empirical correlations of natural convection for the top of a cold plate using Equation 3.4.3.

The flow variables for velocity were set to zero, as only natural convection was modeled. No slip boundary conditions were applied to all fluid-solid interfaces. The fluid layer (air) was modeled as an ideal gas at a reference pressure of 1 atm. The initial condition for temperature was set to 278.7 K, and the numerical simulation was solved for 150 iterations for a convergence criterion of 0.0001. A sample residual plot for one time step is shown in Figure 3-14.

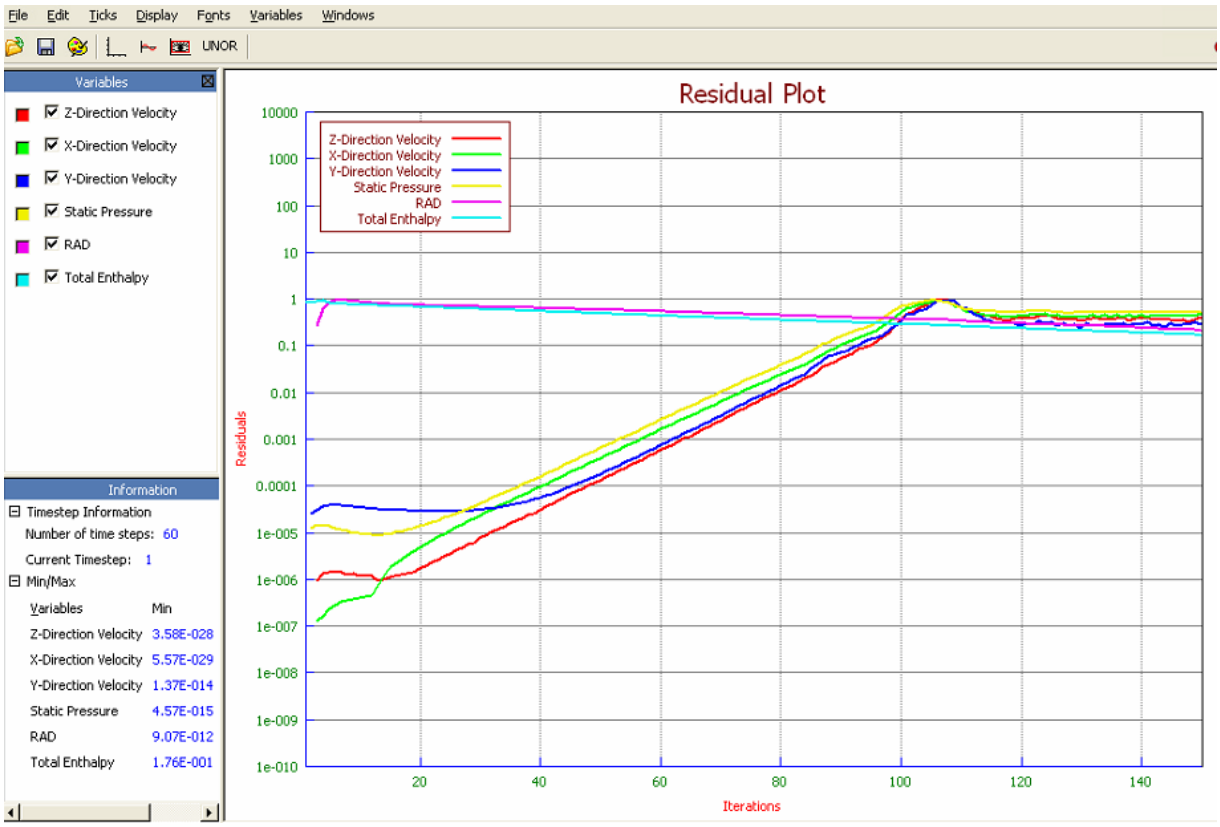

Figure 3-14: Normalized Residual Plot for Transient Simulations

The residual plot of the flow and thermal parameters did not meet the convergence criterion of 0.0001 as can be seen in Figure 3-14. This occurs due to the numerical complexity of solving flow problems dealing with natural convection.

3.5.2 Thermal Results of Transient Simulation

Figure 3-15 and Figure 3-16 show the transient development of the temperature distribution in the model.

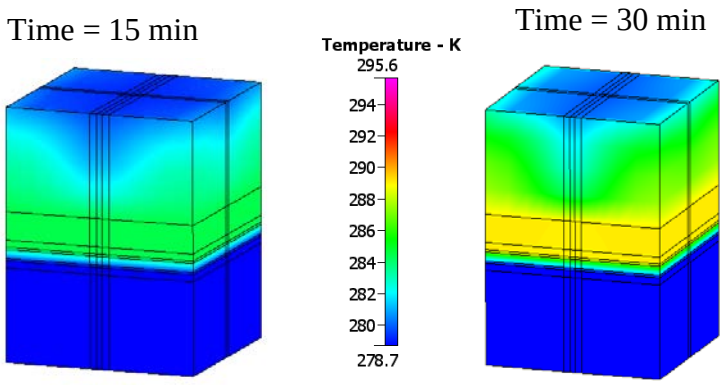

Figure 3-15: Temperature of Transient Simulations

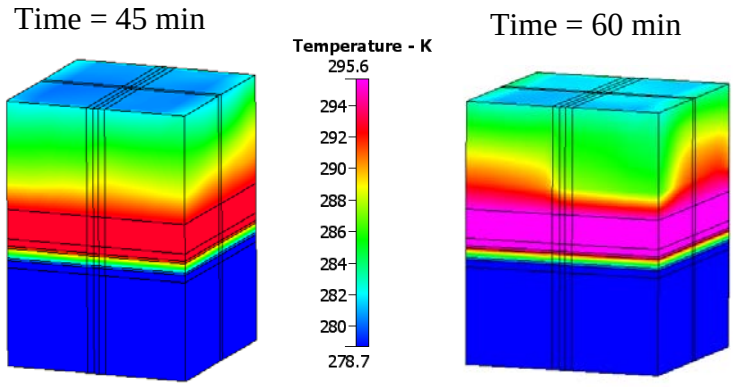

Figure 3-16: Temperature of Transient Simulations

At the end of the transient simulation, a maximum temperature of 295.6 K was obtained, as shown in Figure 3-16. The vector plots showing the direction of natural convection within the fluid layers is shown in Figure 3-17.

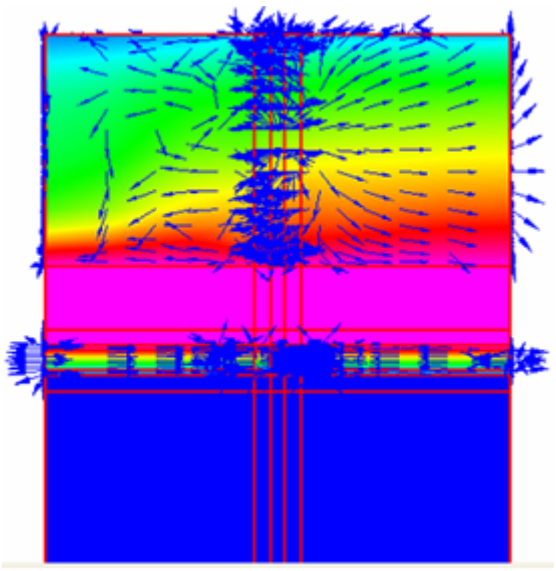

Figure 3-17: Temperature Distribution showing Velocity Vectors of Natural Convection

A closer examination of the temperature distribution across the thermoelectric legs is shown in Figure 3-18 and Figure 3-19.

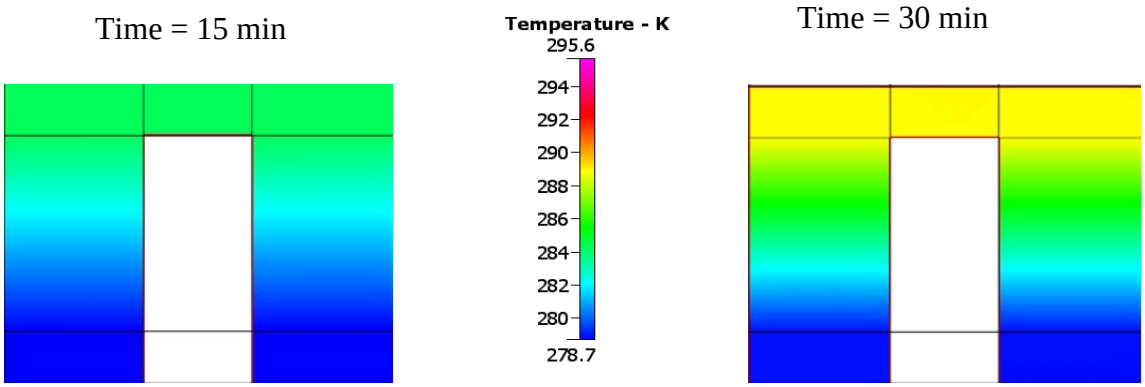

Figure 3-18: Temperature Distribution across Thermoelectric Legs

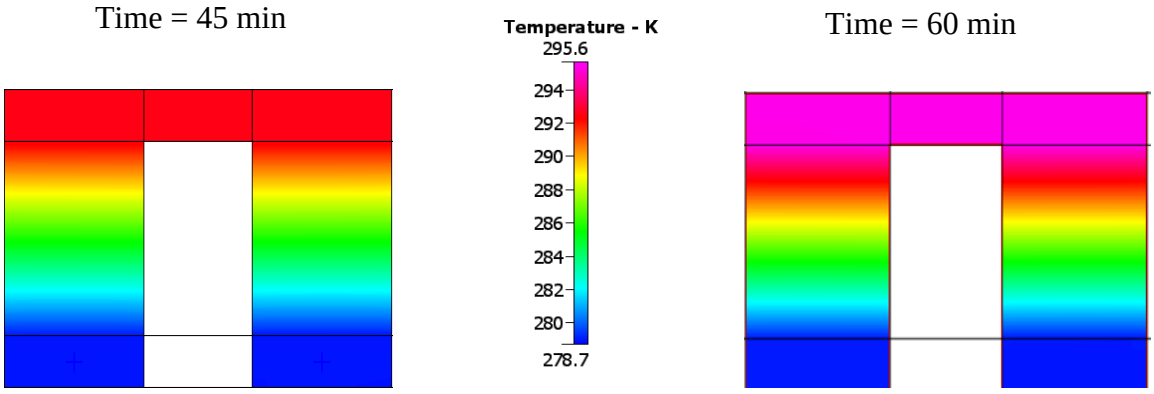

Figure 3-19: Temperature Distribution across Thermoelectric Legs

At the end of the transient simulation, a maximum temperature of 16.5 K was created across the thermoelectric legs.

3.5.3 Electrical Results of Simulation with Fully Coupled Effects

Using the final solution of the transient simulation of flow, heat transfer, and radiation, a steady state simulation of the electric effects for DC conduction was performed over a current range of 0.01 A – 0.14 A. The residual plot of this steady state simulation is shown in Figure 3-20

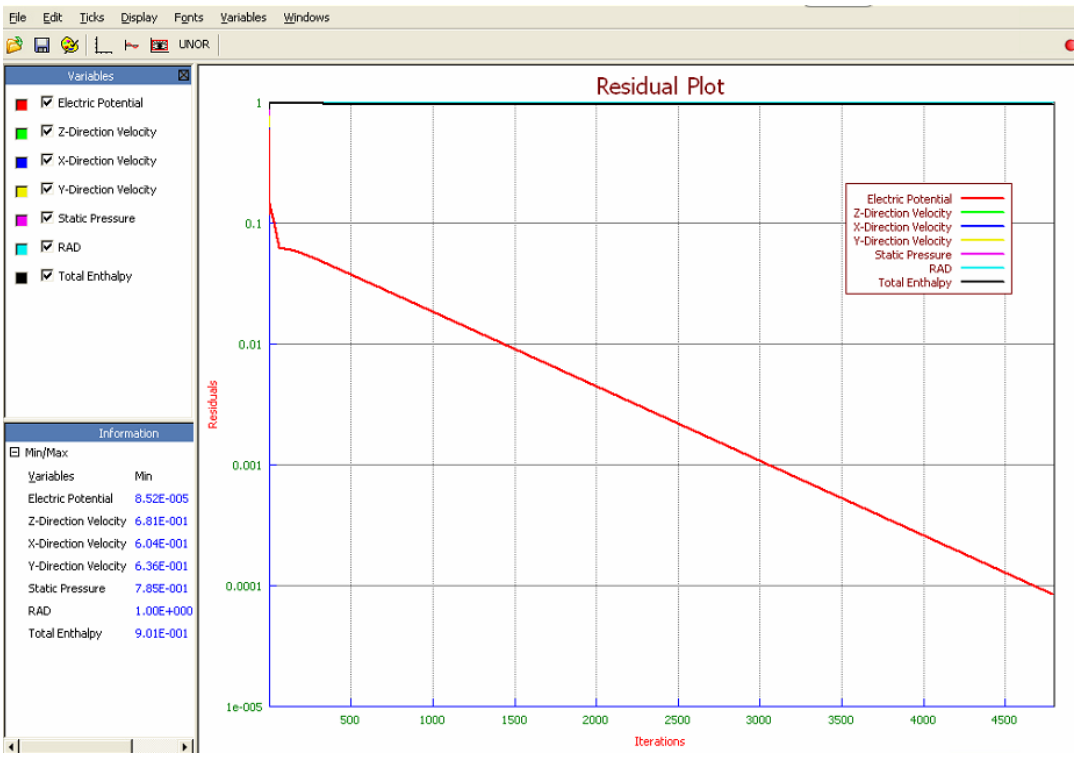

Figure 3-20: Residual Plot of Steady State Electrical Simulation

The voltage distribution across the thermoelectric unicouple corresponding to the maximum power of the thermoelectric module is shown in Figure 3-21.

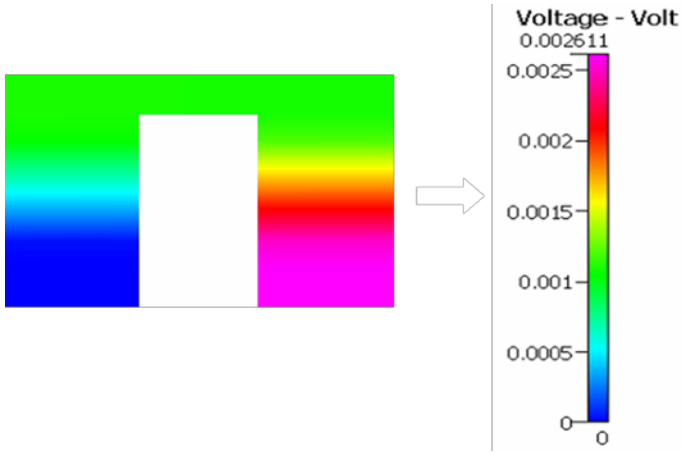

Figure 3-21: Voltage Distribution of Unicouple under Maximum Module Power

The power curve for the fully coupled simulation is shown in Figure 3-22. Again this was generated by multiplying the unicouple voltage by 126, and taking into consideration the contact resistance in 126 unicouples. Here, a maximum power of 0.031 W was obtained. Figure 3-23 illustrates the comparison of the power curves between the fully coupled model and the simulation with prescribed heat transfer coefficients.

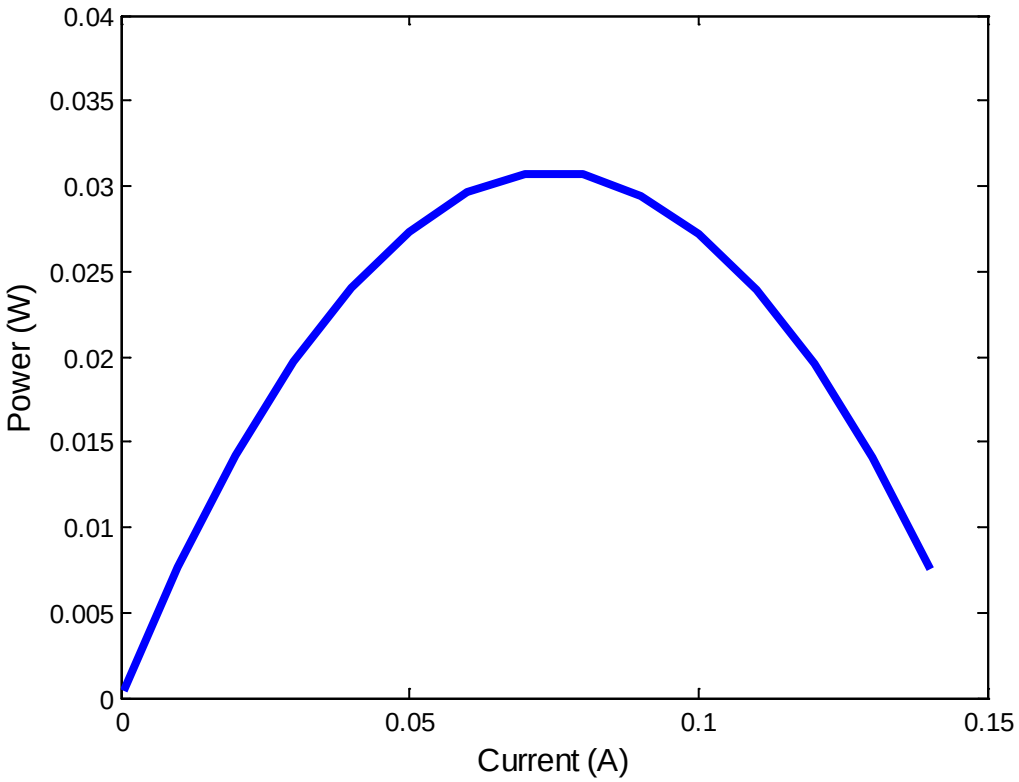

Figure 3-22: Power Curve for Fully Coupled Simulation

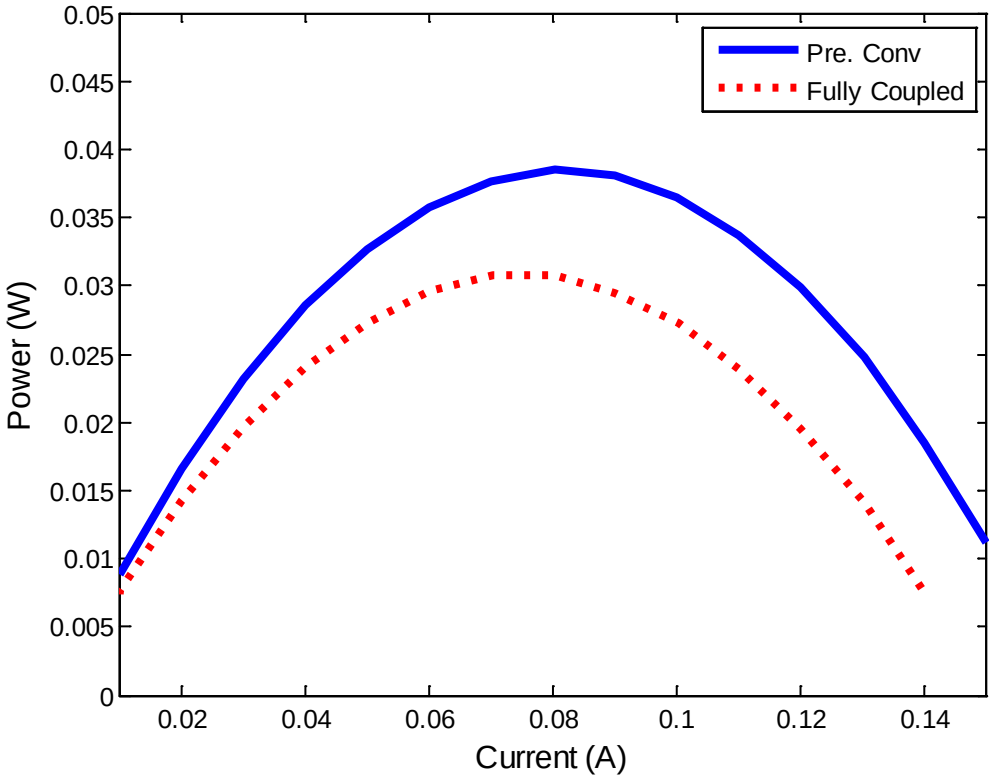

Figure 3-23: Power Curves Comparing Convective and Fully Coupled Models

3.6 Validation of Numerical Solutions

The results of the numerical solution for the fully coupled model were compared to those obtained experimentally. The voltage and power curve comparisons are shown in Figure 3-24 and Figure 3-25 respectively.

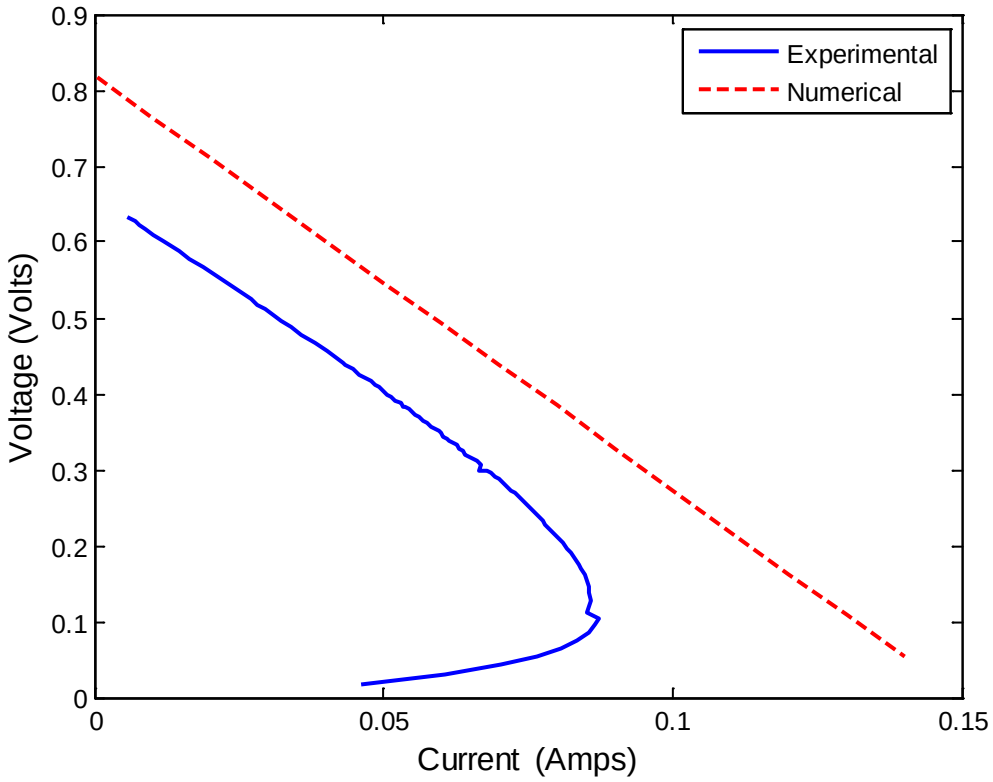

Figure 3-24: Validation of Fully Coupled Voltage Curve

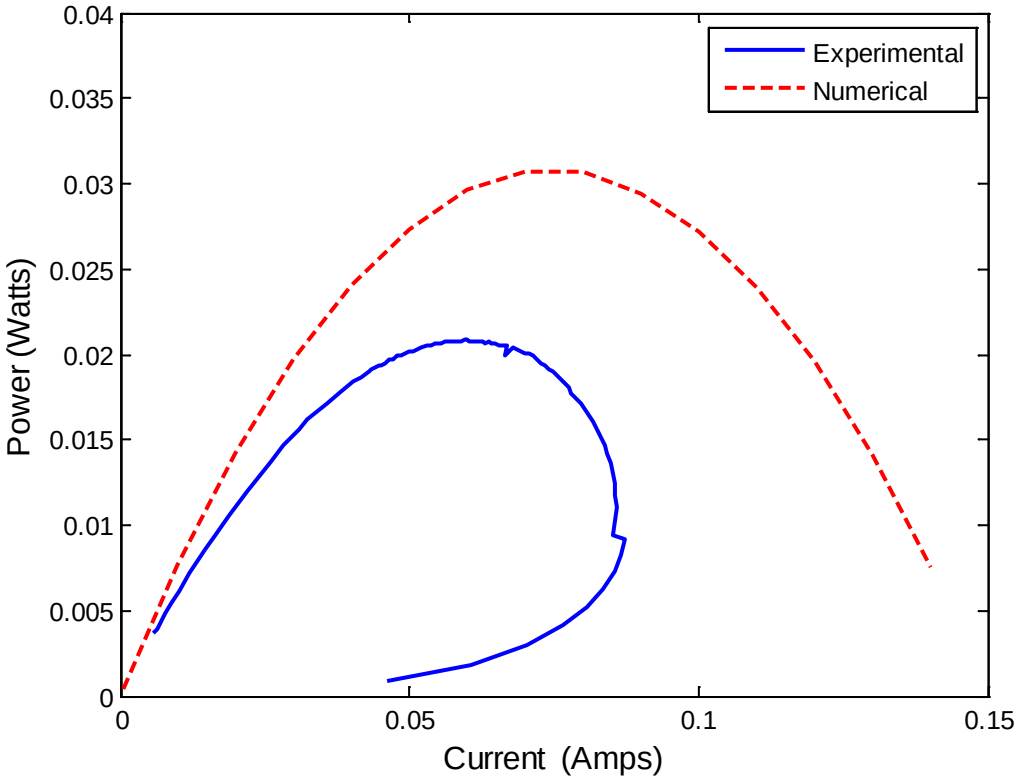

Figure 3-25: Validation of Fully Coupled Power Curve

The calculated peak temperature across the thermoelectric legs was estimated to be approximately 15 K. Here, a maximum temperature of 16.5 K was obtained across the thermoelectric legs. The peak voltage and power obtained in the experiment were 0.66 V and 0.021 W respectively compared to 0.78 V and 0.031 W obtained in the fully coupled simulation.

The disparity between the experimental and the numerical results can be attributed to the following;

- The ambient temperature around which the experiment was conducted outdoors was not recorded, and so the ambient temperature for the numerical model was estimated based on the mid-day temperature for the day the experiment was conducted.
- The STEG in the experimental study was placed within a clear glass box, and exposed to the sun. While the experiment was conducted, the temperature within the glass box was not measured. As a result, the initial temperature conditions used in the transient simulation were assumed to be the same as those of the ambient temperature, assumed to be 278.7 K.
- During the experiment the temperature of the heat sink was not steady. The effect of this was a deviation from a parabolic curve as is seen in the experimental curves. Thus modeling the bottom of the heat sink with an isothermal boundary condition could be inaccurate in reproducing the experimental behavior.

3.7 Effects of Pressure on Fully Coupled Model

An investigation was performed to explore the effects of changing the reference pressure within the fluid layers of the fully coupled model. Reference pressures at 0.5 and 0.1 atm were simulated respectively over 60 times steps for 60 seconds. Lowering the operating pressure was predicted to reduce the convective heat transfer coefficients within the layer of air enclosed in the glass box and in effect, increase the temperature gradient across the thermoelectric legs. The results of the transient simulation at the end of the simulation are shown in Figure 3-26 and Figure 3-27 respectively.

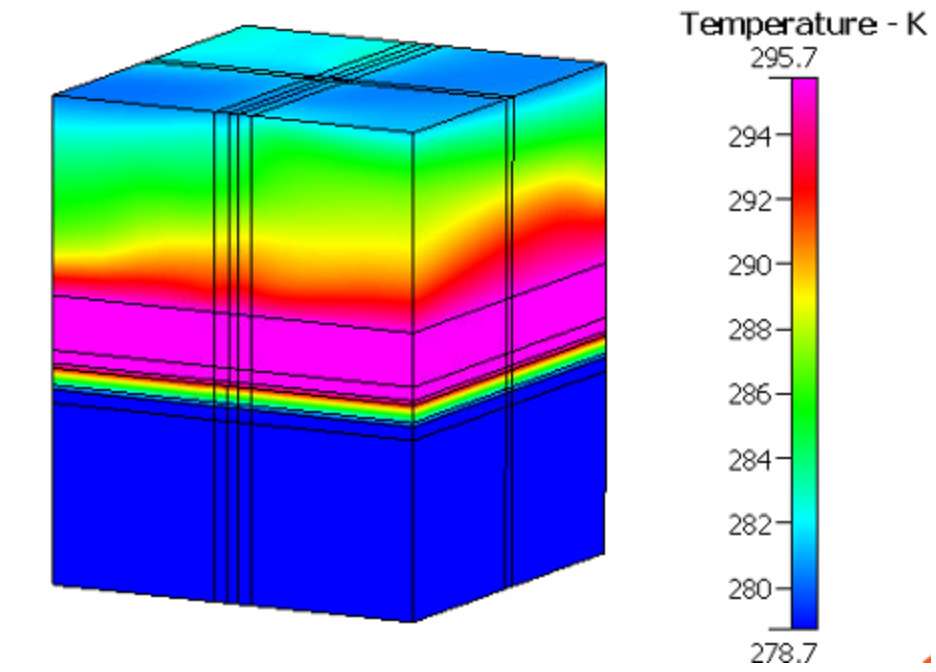

Figure 3-26: Temperature Distribution at 0.5 atm

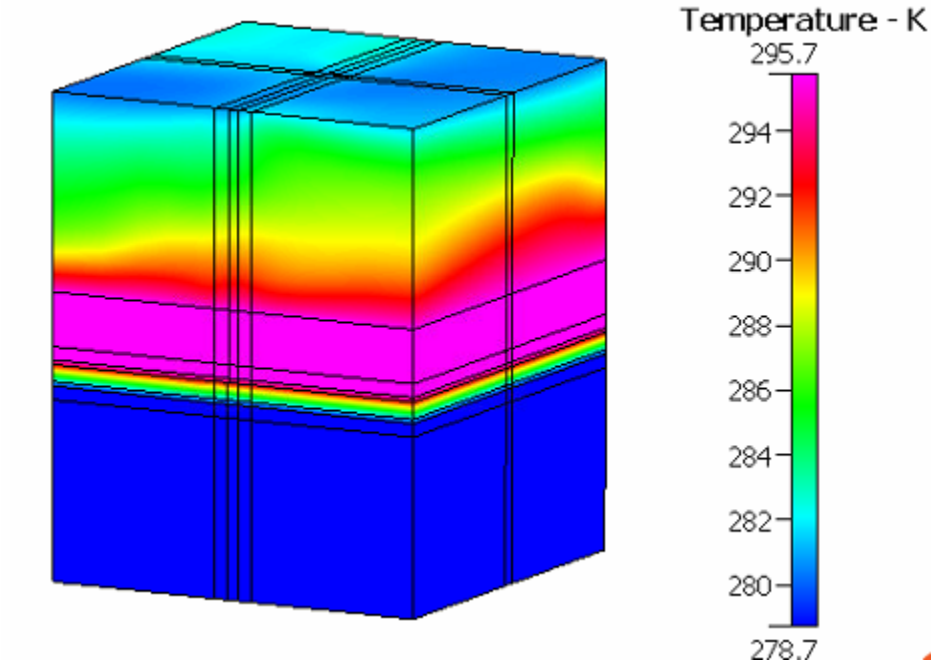

Figure 3-27: Temperature Distribution at 0.1 atm

The thermal results of the pressure variations were not significantly different from those of the fully coupled model at 1 atm. A significant temperature difference could be achieved at much lower operating pressures.

3.8 Calculation of STEG Efficiency

The efficiency of the STEG was computed using the following equations;

$$P_{sun} = q"_{sun} A_{absorber} \quad (3.8.1)$$

$$P_{electric} = IV_{out} \quad (3.8.2)$$

$$\eta_{system} = \frac{P_{electric}}{P_{sun}} \quad (3.8.3)$$

Where P_{sun} is the input solar power, $q"_{sun}$ is the input heat flux, $A_{absorber}$ is the area of the absorber plate used in the experiment, $P_{electric}$ is the electrical power developed by the STEG, I is the current drawn, V_{out} is the output voltage of the STEG, $\eta_{system}$is the system efficiency.

The efficiency of the STEG under different operating conditions can be compared with the efficiency of a Carnot heat engine operating under the same temperature gradients as the thermoelectric device:

$$\eta_{Carnot} = \frac{T_H - T_C}{T_H} \quad (3.8.4)$$

Where η_{Carnot} is the Carnot efficiency, T_H is the hot junction temperature, T_C is the cold junction temperature.

Chapter 4
Summary and Conclusions

This computational study has shown the performance of a flat panel solar thermoelectric generator under different operating conditions. The results of the numerical model under the different conditions investigated are summarized in Table 11 and Table 12. Table 13 provides a comparison with the experimental study.

Table 11: STEG Power under Different Simulated Conditions

Simulated Condition	Maximum Temperature Gradient (K)	Maximum Power Generated (Watts)
Adiabatic	150.3	1.780
Radiative Heat Loss Alone	131.1	1.430
Convective and Radiative Losses	19.5	0.0385
Fully Coupled	16.5	0.031

Table 12: STEG Efficiency under Different Simulated Conditions

Simulated Condition	STEG Efficiency (%)	Carnot Efficiency (%)
Adiabatic	5.14	34.9
Radiative Heat Loss Alone	4.13	31.9
Convective and Radiative Losses	0.111	6.53
Fully Coupled	0.0884	5.58

Table 13: Comparison between Numerical and Experimental Study

	Maximum Temperature Gradient (K)	Maximum Power Generated (Watts)	Efficiency (%)
Fully Coupled Simulation Study	16.5	0.031	0.0884
Experimental Study	□ 15	0.021	0.0582

These results prove that natural convection is the dominant mode of heat loss from the device. In an ideal operation in vacuum, where only heat loss by radiation is present, the numerical model predicts an efficiency of 4.13%, which is approximately 47 times the efficiency obtained under terrestrial conditions. The efficiency obtained for radiative heat losses alone at 4.13%, were in agreement with those obtained in an experimental study at MIT [5].

The numerical result did not match the experimental result, as several assumptions were made for parameters not recorded during the experiment. Nevertheless, it would have provided a close prediction if the heat-sink of the experimental STEG unit was maintained at a constant temperature.

This work can be extended through additional simulations on the effects of pressure at much lower values. Furthermore, parametric studies can be performed on the geometry of the different STEG components, such as the absorber plate and the thermoelectric legs. The results obtained from these studies can provide the information required to optimize the performance of STEGs.

References

1. Lewis, N. et al. Basic *Research Needs for Solar Energy Utilization*. (DOE Office of Science, 2005)
2. Roeb, M. & Muller-Steinhagen, H. Concentrating on Solar electricity and fuels. Science **329**, 773-774 (2010).
3. Mills, D. Advances in solar thermal electricity technology. *Solar Energy 76*, 19-31. 2004.
4. MacDonald, D. K. C., (1962), *Thermoelectricity: An introduction to the principles*, New York: John Wiley & Sons, Inc.
5. Kraemer, D., et al., (2011), "High-performance flat-panel solar thermoelectric generators with high thermal concentration," *Nature Materials*, Vol. 10, pp. 532-8.
6. Modest, M.F., (2003), *Radiative Heat Transfer*, 2nd Edition, Academic Press.
7. Watzman, S., (2013), *Design of a Solar Thermoelectric Generator*, Undergraduate Honors Thesis in Mechanical Engineering, The Ohio State University.
8. *CFD-ACE+*, Developed and licensed by ESI Inc., www.esi-group-na.com
9. Kuo, K.K., (1986), *Principles of Combustion*, Wiley, New York.
10. Bergman, T et. al. *Introduction to Heat Transfer* (2011), John Wiley & Sons, INC.